HPF1-dependent histone ADP-ribosylation triggers chromatin relaxation to promote the recruitment of repair factors at sites of DNA damage

Smith, R.; Zentout, S.; Rother, M.; Bigot, N.; Chapuis, C.; Mihut, A.; ... ; Huet, S.

Citation

Smith, R., Zentout, S., Rother, M., Bigot, N., Chapuis, C., Mihut, A., ... Huet, S. (2023). HPF1-dependent histone ADP-ribosylation triggers chromatin relaxation to promote the recruitment of repair factors at sites of DNA damage. *Nature Structural & Molecular Biology*, *30*(5), 678-691. doi:10.1038/s41594-023-00977-x nature structural & molecular biology

Article

https://doi.org/10.1038/s41594-023-00977-x

HPF1-dependent histone ADP-ribosylation triggers chromatin relaxation to promote the recruitment of repair factors at sites of DNA damage

Received: 27 August 2021

Accepted: 28 March 2023

Rebecca Smith [1,2,7] ✉, **Siham Zentout** [1,7], **Magdalena Rother** [3], **Nicolas Bigot** [1], **Catherine Chapuis** [1], **Alexandra Mihuț** [4,5], **Florian Franz Zobel** [2], **Ivan Ahel** [2], **Haico van Attikum** [3], **Gyula Timinszky** [4] ✉ & **Sébastien Huet** [1,6] ✉

Poly(ADP-ribose) polymerase 1 (PARP1) activity is regulated by its co-factor histone poly(ADP-ribosylation) factor 1 (HPF1). The complex formed by HPF1 and PARP1 catalyzes ADP-ribosylation of serine residues of proteins near DNA breaks, mainly PARP1 and histones. However, the effect of HPF1 on DNA repair regulated by PARP1 remains unclear. Here, we show that HPF1 controls prolonged histone ADP-ribosylation in the vicinity of the DNA breaks by regulating both the number and length of ADP-ribose chains. Furthermore, we demonstrate that HPF1-dependent histone ADP-ribosylation triggers the rapid unfolding of chromatin, facilitating access to DNA at sites of damage. This process promotes the assembly of both the homologous recombination and non-homologous end joining repair machineries. Altogether, our data highlight the key roles played by the PARP1/HPF1 complex in regulating ADP-ribosylation signaling as well as the conformation of damaged chromatin at early stages of the DNA damage response.

PARP1, which belongs to the diphtheria toxin-like family of ADP-ribosyl transferases, is the founding member of a large family of enzymes that regulate a number of different cellular processes. PARP1 itself plays pivotal functions in DNA repair, chromatin folding and gene transcription[1,2]. As part of its role in the DNA damage response (DDR), PARP1 detects both single-strand and double-strand breaks[3] through its amino-terminal DNA-binding domain consisting of three zinc finger modules[4]. The binding of this domain to DNA breaks triggers the catalytic activity of the carboxy-terminal domain via a complex allosteric mechanism[5]. Once activated, PARP1 uses NAD$^+$ to polymerize ADP-ribose (ADPr) chains on target proteins, with the major targets being histones and PARP1 itself[6,7].

Early research into PARP1 focused on its role as a discrete enzyme, capable of catalyzing the addition of ADPr chains alone. However, recent studies identified a key co-factor, HPF1, which is required for targeting ADPr chains on specific residues[8]. Indeed, HPF1 binding to the C terminus of PARP1 creates a joint catalytic site that is essential to ADP-ribosylate serines[9], which are the main residues to be modified by ADPr in the context of the DDR[10]. Consequently, loss of HPF1 has several effects, including strongly reduced automodification of

---

[1] University of Rennes, CNRS, IGDR (Institut de génétique et développement de Rennes) - UMR 6290, BIOSIT – UMS3480, Rennes, France. [2] Sir William Dunn School of Pathology, University of Oxford, Oxford, UK. [3] Department of Human Genetics, Leiden University Medical Center, Leiden, the Netherlands. [4] Laboratory of DNA Damage and Nuclear Dynamics, Institute of Genetics, Biological Research Centre, Eötvös Loránd Research Network (ELKH), Szeged, Hungary. [5] Doctoral School of Multidisciplinary Medical Sciences, University of Szeged, Szeged, Hungary. [6] Institut Universitaire de France, Paris, France. [7] These authors contributed equally: Rebecca Smith, Siham Zentout. ✉e-mail: rebecca.smith@path.ox.ac.uk; timinszky.gyula@brc.hu; sebastien.huet@univ-rennes.fr

PARP1 and the suppression of *trans*-ADP-ribosylation of histones[11,12]. Moreover, in vitro, HPF1 is not only required for targeting ADPr to specific residues, but it also controls the rate of polymerization, favoring mono-ADPr modifications over poly-ADPr chains[13].

The major findings reported over the past few years have considerably improved our understanding of the molecular mechanisms underlying the control of ADP-ribosylation signaling by the PARP1/HPF1 axis. Nevertheless, the exact effect of HPF1 on cellular functions known to be regulated by PARP1 remains unclear. A role for HPF1 in DNA repair has been hinted at, as HPF1 deficiency led to cell hypersensitivity to DNA-damaging agents[8]. In this report, we aimed to further investigate how HPF1 could regulate ADP-ribosylation-dependent steps of the DDR. We show that HPF1 is recruited to DNA lesions via its binding to the C-terminal residues of PARP1 and that it controls both the number and length of ADPr chains at sites of damage. We also establish that HPF1-dependent histone ADP-ribosylation, rather than PARP1 automodification, is a major trigger of the early chromatin unfolding that occurs at sites of damage and which facilitates access to the damaged DNA for repair factors. Thus, we demonstrate that HPF1 is a central player at early stages of the DDR and that its role in the regulation of chromatin structure contributes to efficient DNA repair.

Results

HPF1 recruits to sites of damage via a PARP1 interaction

HPF1 has been shown to be recruited to sites of DNA damage[8], but the mechanism driving its recruitment has yet to be fully elucidated. Although it was proposed that this recruitment relies on HPF1 interaction with the C terminus of PARP1, and in particular its last two residues L1013/W1014 (refs. 9,14), other results suggested that HPF1 and PARP1 accumulate at sites of damage independently from each other[15]. To investigate this question, we aimed to better characterize the dynamic behavior of HPF1 at DNA lesions. First, in agreement with previous findings[8], we found that HPF1 accumulated at sites of laser microirradiation-induced DNA damage (Extended Data Fig. 1a), and was enriched in the chromatin-bound fraction together with PARP1 after H_2O_2 treatment (Extended Data Fig. 1b). In addition, proximity ligation assays showed the accumulation of both PARP1 and HPF1 at DNA double-strand breaks (DSBs) induced by X-ray irradiation (Extended Data Fig. 1c–f).

We then compared the recruitment kinetics of both HPF1 and PARP1 to sites of damage induced by laser microirradiation in U2OS *PARP1^KO* cells co-expressing mCherry-PARP1 and GFP-HPF1 (Fig. 1a,b). Although the recruitment of both proteins peaked within 10 s, we observed that PARP1 accumulation to sites of damage was much stronger than HPF1. This difference in the relative amounts of the two proteins accumulating at DNA lesions is in line with in vitro data suggesting that HPF1 can exert its regulatory role on PARP1 even at low relative molarity[16]. Following the rapid recruitment phase, HPF1 dissipated from the damage slower than PARP1 (Fig. 1b,c and Extended Data Fig. 1g). This slow dissipation was not affected by the level of ectopic expression of GFP-tagged HPF1 (Extended Data Fig. 2a–e), nor by the presence of endogenous HPF1 (Extended Data Fig. 2f), ruling out an artifact associated with the overexpression of GFP-HPF1. The differential release speed of PARP1 and HPF1 implies that the HPF1/PARP1 molarity ratio increases progressively after DNA damage induction, which could explain the slower wave of histone ADP-ribosylation compared with PARP1 automodification observed by western blot analysis in cells treated with H_2O_2 (Fig. 1d).

In agreement with previous results[8], we found that PARP1 deficiency nearly fully suppressed HPF1 recruitment to DNA lesions, with the presence of PARP2 being unable to compensate for PARP1 loss despite the known interaction between HPF1 and PARP2 (Fig. 1e and Extended Data Fig. 2g). HPF1 recruitment in *PARP1^KO* cells was rescued upon re-expression of a wild-type version of PARP1 (PARP1 WT) but not in the presence of PARP1 mutated at residues L1013A/W1014A (PARP1 LW/AA) (Fig. 1e). These data indicate that the interaction of HPF1 with these last two PARP1 residues is critical for HPF1 accumulation to sites of damage. We also observed that PARP1 tagged at its C-terminal end is unable to rescue HPF1 recruitment when expressed in *PARP1^KO* cells. Therefore, this tagging strategy should be avoided when assessing PARP1 behavior at sites of damage (Extended Data Fig. 2h).

Besides its recruitment to sites of DNA damage, we also wondered whether HPF1 release could be regulated by the mobilization of PARP1 from this area. Auto-ADP-ribosylation of PARP1 is a key regulator of its release from the DNA lesions[17]. Therefore, we analyzed HPF1 release in *PARP1^KO* cells re-expressing PARP1 mutants displaying impaired auto-ADP-ribosylation (Extended Data Fig. 2i–k) due to either suppressed catalytic activity (PARP1 E988K) or mutations of the main serine residues targeted for ADP-ribosylation on PARP1 (PARP1 S499/507/519A, PARP1 3SA). As previously shown[17–19], both mutants were retained longer at sites of damage than PARP1 WT, and we observed that HPF1 release kinetics mirrored the relative dissipation speeds of the different PARP1 mutants (Fig. 1f–h and Extended Data Fig. 2l,m). In line with these findings, the accumulation of endogenous or GFP-tagged HPF1 at sites of DNA damage a few minutes after laser irradiation appeared enhanced in cells treated with PARP inhibitors that trap PARP1 at these lesions (Extended Data Fig. 1a). These results highlight that the transient accumulation of HPF1 at damage sites is tightly controlled by PARP1 during both the accumulation and release phases.

HPF1 controls the characteristics of ADP-ribose chains

HPF1 controls both the targeting of ADPr chains on specific residues and the rate of ADP-ribosylation[11,16]. Therefore, we investigated the overall effect of the loss of HPF1 on ADP-ribosylation signaling at sites of damage by analyzing the recruitment kinetics of two different ADPr-binding domains. First, the macrodomain of macroH2A1.1, which associates with mono-ADPr or the terminal residue of poly-ADPr chains[20,21] (Fig. 2a), was used as a proxy for the number of ADPr chains at sites of damage. Second, the WWE domain of RNF146, which binds at the interface between two monomers along poly-ADPr chains, was used to estimate the total amount of ADPr[22] (Fig. 2a). Both ADPr-binding

Fig. 1 | HPF1 recruitment to sites of damage relies on interaction with the C terminus of PARP1. a, Representative images of mCherry-PARP1 and GFP-HPF1 recruitment to sites of DNA damage induced by 405 nm laser irradiation, in *PARP1^KO* cells. Scale bar, 5 µm. **b**, Recruitment kinetics of mCherry-PARP1 (black) and GFP-HPF1 (red) to sites of DNA damage. **c**, To assess the relative release kinetics of mCherry-PARP1 and GFP-HPF1, the time of maximum accumulation (t_{max}) and the time at which half of PARP1 has been released compared with maximum accumulation ($t_{1/2}$) were first estimated from the mean curve shown in **b**. Then, for each individual recruitment curve of mCherry-PARP1 and GFP-HPF1, the residual accumulation was measured as the ratio between the recruitment intensities at $t_{1/2}$ and t_{max}. Data in **b** and **c** are representative of three independent replicates where data were collected from 11 cells. **d**, Western blot displaying ADPr signals, stained with a pan-ADPr antibody in cells treated with H_2O_2 collected at the indicated time points after treatment. PARP1 and histone ADPr are indicated by arrows on the right of the image. PARP1 and tubulin were used as loading controls. NT, no treatment. **e**, Recruitment kinetics of GFP-HPF1 to sites of DNA damage in *WT* or *PARP1^KO* cells expressing mCherry-tagged PARP1 WT or PARP1 L1013A/W1014A (PARP1 LW/AA). Data in **e** are representative of three independent replicates where data were collected from 15–16 cells per condition. **f**,**g**, Recruitment kinetics of mCherry-PARP1 3SA (black) (**f**) or mCherry-PARP1 E988K (black) (**g**) and GFP-HPF1 (red) to sites of DNA damage. **h**, From the mean recruitment curve of mCherry-tagged PARP1 WT expressed in *PARP1^KO* cells, t_{max} and $t_{1/2}$ were first estimated. Then, for each individual recruitment curve of mCherry-tagged PARP1 mutants and GFP-HPF1, the residual accumulation is measured as the ratio between the recruitment intensities at $t_{1/2}$ and t_{max}. Data in **f**–**h** are representative of three independent replicates where data were collected from 13–18 cells per condition.

domains showed similar behavior upon laser irradiation: an initial peak of recruitment within the first 30 s after damage, followed by a stable or slowly decreasing plateau within the next 10 min (Fig. 2b–e). These recruitment profiles suggest that ADP-ribosylation signaling starts with an early acute phase, followed by a more sustained period lasting for several minutes after damage. Importantly, this prolonged signaling phase arises from a dynamic equilibrium between ADPr polymerase and hydrolase activities, as the acute inhibition of PARP1 during this period leads to the rapid removal of the ADPr chains from the sites of damage[23].

We found that HPF1 deficiency was associated with a strong reduction in macrodomain recruitment (Fig. 2b,c). A similar defect was observed in *PARP1*^{KO} cells expressing PARP1 LW/AA, which is unable

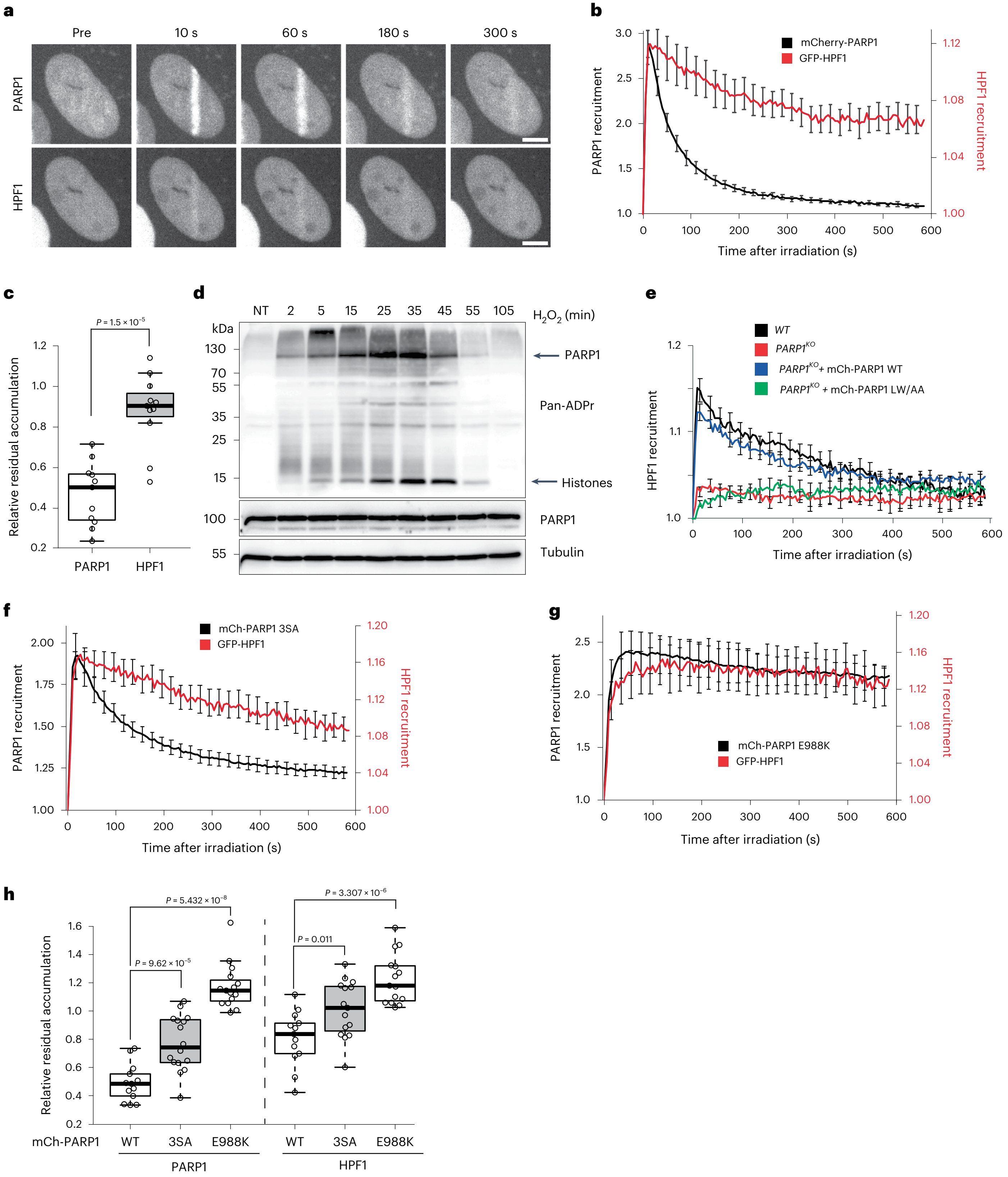

to recruit HPF1 to DNA lesions, compared with those expressing PARP1 WT (Extended Data Fig. 3a,b). Using a pan-ADPr antibody, which binds to both mono-ADPr and poly-ADPr similar to the macrodomain of macroH2A1.1 used with laser microirradiation, we also monitored the ADPr signal at bona fide DSBs induced at a stably integrated lactose operator (LacO) array by the FokI nuclease fused to the lactose repressor (LacR) (Fig. 2f). Knockdown of HPF1 led to reduced pan-ADPr staining at DSBs (Fig. 2g–i). Collectively, these analyses consistently show that the absence of HPF1 leads to a decrease in the number of ADPr chains that are generated at DSBs. Conversely, HPF1 deficiency had no major effect on WWE accumulation to sites of laser irradiation (Fig. 2d,e), showing that the total amount of ADPr generated at sites of damage remained unchanged. This, together with the data regarding macrodomain recruitment or pan-ADPr staining, suggests that the fewer chains generated in the absence of HPF1 are longer. Altogether, our findings agree with previous in vitro results showing that HPF1 is not only crucial to initiate the formation of ADPr chains on a substantial number of acceptor residues, but also restrains ADPr chain length[13].

Recent reports have also shown that modifying the relative molarities of HPF1 and PARP1 strongly affects ADP-ribosylation activity in vitro[13,16]. Therefore, we wondered what the effect would be of the overexpression of HPF1, whose endogenous nuclear level is 20 to 50 times lower than that of PARP1[8], on ADP-ribosylation signaling at sites of damage. HPF1 overexpression had little influence on the initial peak of both macrodomain and WWE but perturbed the slower plateau phases (Fig. 2j,k) with increased accumulation of macrodomain while WWE was reduced at sites of damage. These results were confirmed by immunoblotting, which showed that HPF1 overexpression enhanced pan-ADPr staining while reducing poly-ADPr signals upon genotoxic stress induced by H_2O_2 (Fig. 2l). Therefore, excess HPF1 appears to increase the amount of ADPr chains while reducing their lengths. These data show that the relative amounts of HPF1 versus PARP1 within the nucleus controls the characteristics of ADP-ribosylation signaling at sites of damage.

HPF1 regulates chromatin relaxation at sites of DNA damage

In addition to its role in signaling the presence of DNA lesions for repair effectors, ADP-ribosylation by PARP1 also triggers rapid chromatin relaxation in the vicinity of DNA breaks[24], a process that facilitates access to the lesions[23]. Therefore, we wondered whether HPF1 could also regulate this early chromatin remodeling process because of its regulatory role in ADP-ribosylation signaling. We monitored the amount of chromatin relaxation in *WT*, *PARP1*^{KO}, *HPF1*^{KO} and *PARP1*^{KO}/*HPF1*^{KO} cells by a live-cell chromatin relaxation assay (Fig. 3a–c). In this assay, a region of chromatin is highlighted by the local photoactivation of PAGFP fused to the histone H2B, which occurs simultaneously to damage induction by laser irradiation at 405 nm. The changes in the level of chromatin condensation at the sites of damage are estimated by measuring the thickness of the photoactivated line. Chromatin relaxation at sites of damage was nearly fully suppressed in the absence of PARP1. The loss of HPF1 also dramatically reduced chromatin relaxation, although not to the same degree as in *PARP1*^{KO} cells. We observed similar impairment of chromatin relaxation in HPF1-deficient cells when using a femtosecond-pulsed infrared laser to induce DNA lesions in non-presensitized cells (Extended Data Fig. 4a). Interestingly, the concomitant loss of PARP1 and HPF1 led to relaxation levels that were lower than those in *HPF1*^{KO} cells, showing that the residual relaxation seen in these cells remains PARP1 dependent (Fig. 3c). This defect in chromatin relaxation seen in *HPF1*^{KO} cells is the consequence of the absence of HPF1 at DNA lesions. Indeed, the expression in *PARP1*^{KO} cells of the PARP1 LW/AA mutant or C-terminally tagged PARP1, which both fail to recruit HPF1 to sites of damage, was unable to restore chromatin relaxation at the level measured in cells re-expressing PARP1 WT (Fig. 3d and Extended Data Fig. 4b). Similarly, the expression of the HPF1 mutant D283A, which does not recruit to damage (Extended Data Fig. 4c) because of an impaired interaction with PARP1[9,14], did not rescue chromatin relaxation in *HPF1*^{KO} cells (Fig. 3e).

To address the effect of HPF1 on the chromatin compaction state at bona fide DSBs, we monitored the size of the LacO array in cells expressing the FokI-LacR fusion protein and found that HPF1 knockdown, similar to PARP inhibitor treatment, reduced the size of the LacO array (Fig. 3f,g). Therefore, chromatin appeared more compact at DSBs following HPF1 depletion or upon inhibition of ADP-ribosylation signaling, which is in line with our observations seen with laser microirradiation-induced DNA damage. Images of undamaged nuclei stained with Hoechst did not show significant differences in chromatin patterns between *HPF1*^{KO} and *WT* cells (Extended Data Fig. 4d,e), ruling out the possibility that the defect in chromatin compaction state at DNA lesions upon HPF1 loss would result from impaired chromatin conformation prior to damage.

Interestingly, we also found that the overexpression of wild-type HPF1 led to a dramatic increase of DNA damage-induced chromatin relaxation (Fig. 3h). Nevertheless, this massive unfolding of the chromatin structure remains reversible, similar to that in cells with endogenous HPF1 levels. Indeed, a progressive recondensation of the chromatin structure was also observed in HPF1-overexpressing cells following the initial rapid relaxation phase, where approximately 30 min after irradiation the chromatin compaction levels were similar to their pre-damage state. Monitoring the chromatin compaction and HPF1 accumulation at sites of laser irradiation in parallel showed that the chromatin recondensation phase follows a time course similar to that observed for HPF1 release (Extended Data Fig. 4f). Thus, the slow dissipation of HPF1 from the lesions could be associated with a progressive loss of HPF1-dependent ADPr signaling, which would in turn lead to a recovery of the chromatin compaction state. Altogether, these findings reveal that HPF1 plays a central role in the PARP1-dependent chromatin remodeling events occurring at early stages of the DDR.

Chromatin relaxation requires ADP-ribosylation of histones

To further investigate the mechanisms underlying the regulation of chromatin remodeling by HPF1 at sites of DNA damage, we first analyzed

Fig. 2 | HPF1 regulates ADP-ribosylation signaling at sites of DNA damage. **a**, Schematic representation of WWE and macrodomain recruitment on ADPr chains. **b**, Representative images showing recruitment of the macrodomain of macroH2A1.1 to DNA damage induced by 405 nm laser irradiation in *WT* and *HPF1*^{KO} cells. Scale bar, 5 µm. **c**, Recruitment kinetics of the macrodomain to sites of DNA damage in *WT* (black) and *HPF1*^{KO} (red) cells. Data in **c** are representative of three independent replicates where data were collected from 11–12 cells per condition. **d**, Representative images showing recruitment of the WWE domain of RNF146 to sites of 405 nm laser-induced DNA damage in *WT* and *HPF1*^{KO} cells. Scale bar, 5 µm. **e**, Recruitment kinetics of the WWE domain to sites of DNA damage in *WT* (black) and *HPF1*^{KO} (red) cells. Data in **e** are representative of three independent replicates where data were collected from 10 cells per condition. **f**, Schematic of the assay used to locally induce bona fide DSBs via the tethering of the FokI endonuclease fused to a LacR at the stably integrated LacO array in U2OS 2-6-3 cells. **g**, Pan-ADPr and γH2AX signals in U2OS 2-6-5 cells with DSBs at the LacO array via the expression of the mCherry-LacI-FokI fusion. Inset shows magnified view of the LacO array. **h**, Quantification of pan-ADPr signal at LacO array in control and HPF1-depleted cells. Data in **h** are representative of three independent replicates where data were collected from 46–59 cells per condition. **i**, Western blot showing HPF1 depletion efficiency upon siRNA transfection. Tubulin is used as a loading control. **j**,**k**, Recruitment kinetics of GFP-macrodomain of macroH2A1.1 (**j**) or GFP-WWE domain of RNF146 (**k**) at sites of DNA damage in U2OS *WT* cells overexpressing mCherry-HPF1 or not. Data are shown as mean ± s.e.m. Data in **j** and **k** are representative of three independent replicates where data were collected from 11–18 cells per condition. **l**, Western blot displaying pan-ADPr and poly-ADPr signals in cells expressing unfused GFP or GFP-HPF1 and treated or not with H_2O_2. Blots were also stained against PARP1, HPF1 and GFP. Tubulin and H2B were used as loading controls.

the behavior of the HPF1 mutant E284A, which interacts with PARP1 but blocks the ADP-ribosylation activity of the joined catalytic site created by the PARP1/HPF1 heterodimer[9]. Although this E284A mutant displayed increased recruitment to DNA lesions compared with wild-type HPF1 (Extended Data Fig. 4c) in line with its tighter binding to PARP1[13], it was unable to rescue ADP-ribosylation signaling (Extended Data Fig. 5a) nor the chromatin relaxation defects observed in *HPF1*^{KO} cells (Fig. 4a). This finding demonstrates that the ADP-ribosylation activity of the PARP1/HPF1 complex is needed for chromatin remodeling at sites of damage.

Upon DNA damage, HPF1 has been shown to control the addition of ADPr moieties on serine residues of specific targets[10]. This includes not only auto-ADP-ribosylation of PARP1 itself, but also *trans*-ADP-ribosylation of other targets, in particular histones, which are the main ADP-ribosylation targets after PARP1[10]. Therefore, we assessed the relative contributions of the ADP-ribosylation of PARP1 and the histones to the HPF1-dependent chromatin relaxation observed at sites of damage. First, we found that the PARP1 3SA mutant, which can still catalyze histone ADP-ribosylation due to interaction with HPF1[17] but shows greatly reduced auto-ADP-ribosylation (Extended

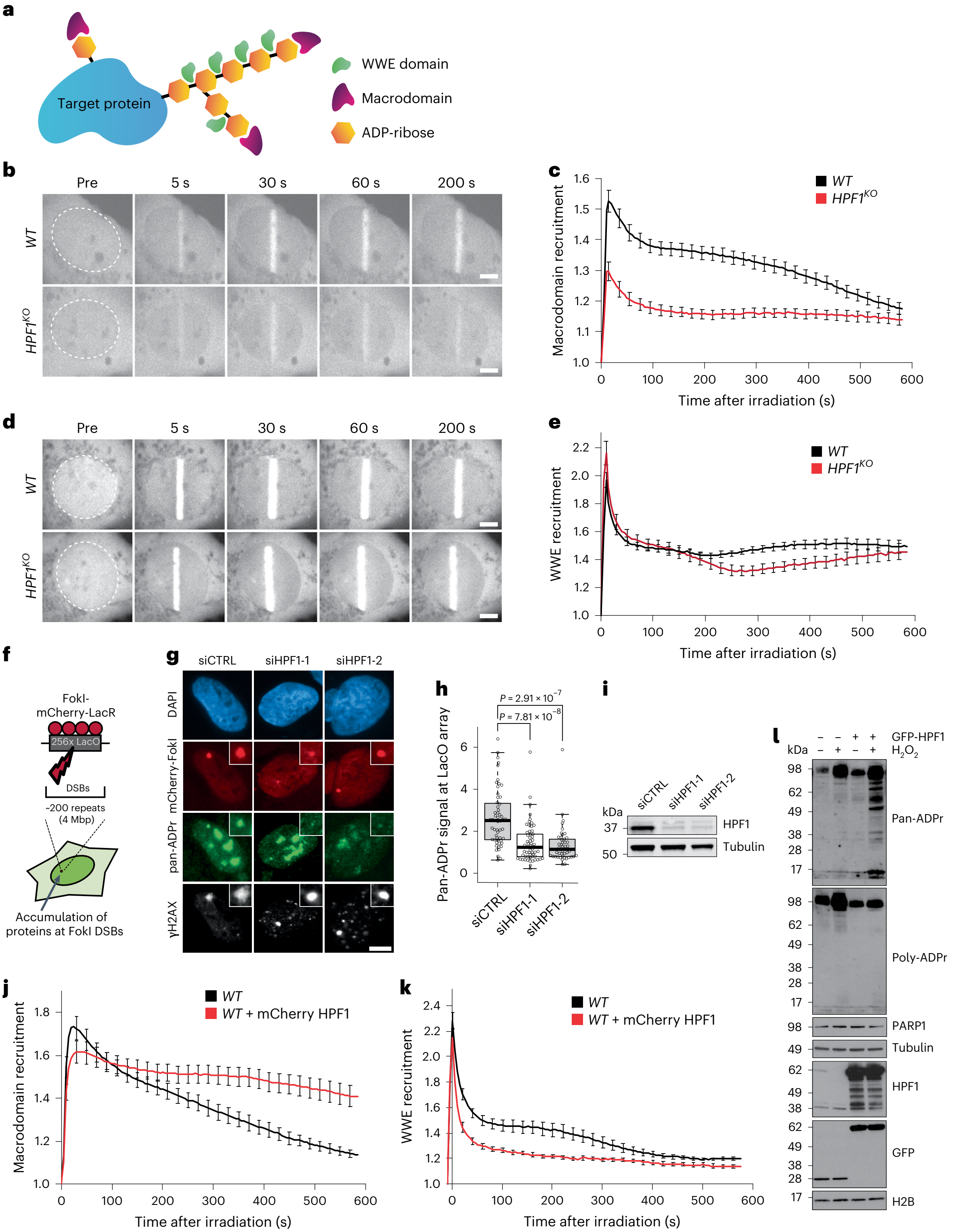

Data Figs. 2i–k and 5b), restored chromatin relaxation in *PARP1^{KO}* cells similar to PARP1 WT complementation (Fig. 4b). As expected, this rescue relied on the presence of HPF1, as expressing PARP1 3SA in *PARP1^{KO}*/*HPF1^{KO}* cells did not permit chromatin relaxation to reach the level observed in *WT* cells. Next, we analyzed the behavior of the HPF1 mutant R239A at DNA lesions. In agreement with in vitro observations showing that this mutation does not significantly affect the interaction with PARP1[14], we observed that HPF1 R239A was recruited to DNA lesions, although at a lower level than its wild-type counterpart (Extended Data Fig. 5c,d). Furthermore, this mutation perturbed the catalytic activity of the PARP1/HPF1 complex by preventing histone ADP-ribosylation while preserving some PARP1 automodification (Fig. 4c), confirming previous reports[9,14]. When expressed in *HPF1^{KO}* cells, the HPF1 R239A mutant was unable to promote chromatin relaxation as observed with wild-type HPF1 complementation (Fig. 4d). Together with the results regarding the PARP1 3SA mutant, these findings indicate that the driving force for chromatin remodeling at sites of damage is the ADP-ribosylation of histones rather than of PARP1.

Finally, given that several chromatin remodelers were found to recruit to DNA lesions and contribute to chromatin remodeling at sites of damage[24–26], we wondered whether the chromatin relaxation promoted by histone ADP-ribosylation relied on ATP-dependent processes. ATP deprivation, which leaves ADP-ribosylation signaling mostly unaffected at sites of damage (Extended Data Fig. 5e)[24], did not prevent the dramatic increase in chromatin relaxation observed upon overexpression of HPF1 (Fig. 4e). The increased relaxation upon HPF1 overexpression was also found in cells knocked out for ALC1 or CHD7, both of which are remodelers that have been shown to contribute to chromatin unfolding at early stages of the DDR[24,25] (Extended Data Fig. 5f–i). Therefore, although subsequent ATP-dependent remodeling processes are also needed, histone ADPr itself appears sufficient to initiate chromatin relaxation at sites of damage.

HPF1-driven chromatin relaxation facilitates access to DNA

In our previous work, we have shown that ADP-ribosylation-dependent chromatin unfolding promotes access to DNA at sites of damage[23]. Because HPF1 appears to be a key regulator of the chromatin relaxation process, we wondered whether this factor could also regulate DNA accessibility in the vicinity of DNA lesions. To address this question, we used the BZIP domain of the transcription factor C/EBPa as a sensor of DNA accessibility[23]. This domain dynamically binds to DNA throughout the nucleus and rapidly accumulates at sites of DNA damage because of increased access to DNA in this area[23] (Fig. 5a). Therefore, the reduced accumulation of BZIP in *HPF1^{KO}* cells (Fig. 5a–c) demonstrated that HPF1 facilitates access to DNA at sites of damage. We also monitored DNA accessibility in the absence of damage in *WT* and *HPF1^{KO}* cells by measuring the nuclear dynamics of BZIP by fluorescence correlation spectroscopy (FCS), considering that increased DNA access enhances BZIP binding to DNA and thus reduces the motion of this sensor in the nucleus[23]. No difference in diffusion coefficient could be observed for BZIP between undamaged *WT* and *HPF1^{KO}* cells (Fig. 5d,e), indicating that DNA accessibility is similar between the two cell lines prior to DNA damage. This is in line with an absence of detectable differences in chromatin conformation between *WT* and *HPF1^{KO}* cells (Extended Data Fig. 4d,e).

Finally, we wondered whether the increased exposure of DNA was an intrinsic property of the unfolded chromatin state promoted by HPF1-dependent histone ADP-ribosylation, irrespective of the presence of DNA lesions. To test this, we made use of the observation that cells lacking the serine ADP-ribosylhydrolase ARH3 show strong spontaneous activation of ADP-ribosylation signaling when compared with *WT* cells upon inhibition of the poly(ADP-ribose) glycohydrolase (PARG), particularly on histones (Fig. 5f)[27]. Importantly, other DNA-damaging signaling pathways are not activated under this condition[27], showing that the enhanced ADP-ribosylation signaling associated with this co-inhibition is not the consequence of increased levels of spontaneous DNA lesions. The DNA-binding sensor BZIP displayed slower nuclear diffusion in PARGi-treated *ARH3^{KO}* cells than in PARGi-treated *WT* cells, indicating enhanced binding to DNA in the *ARH3^{KO}* cells (Fig. 5g). Therefore, these findings show that histone ADP-ribosylation leads to a chromatin conformation characterized by more accessible DNA regardless of the activation of the DDR.

HPF1-driven chromatin relaxation promotes DNA-binding repair factor recruitment

Next, we wondered whether the reduced DNA accessibility at sites of damage in *HPF1^{KO}* cells could impair the recruitment of factors that are involved in DNA repair, in manner similar to that observed for the DNA-binding domain BZIP. We focused on the following proteins: ZNF384, ZMYM3, E4F1, CHD4 and CHD7. Indeed, although they have different roles during DNA repair, their accumulation to sites of damage share the same two features: (1) it relies on their ability to bind DNA and (2) it is ADP-ribosylation dependent[25,26,28–30]. Moreover, for ZNF384, CHD4 and CHD7, it was shown that ADP-ribosylation-dependent chromatin relaxation, rather than direct binding to ADPr, promotes their recruitment to DNA lesions[25,26,28].

Monitoring the recruitment kinetics of these factors, we found that they recruited to damage much slower than the ADPr-binding domains and rather followed a time course resembling that of chromatin unfolding at DNA lesions (Figs. 3b and 6a–f and Extended Data Fig. 6). Additionally, the accumulation of all of these factors to sites of damage was reduced upon HPF1 loss and was further impaired in *PARP1^{KO}* cells or upon treatment with PARP inhibitors, mirroring the reduction in chromatin relaxation observed in *HPF1^{KO}* and *PARP1^{KO}* cells compared with *WT* cells (Fig. 6a–f and Extended Data Fig. 6). Finally, the expression of PARP1 3SA, but not PARP1 LW/AA, in *PARP1^{KO}* cells was able to rescue the recruitment of ZMYM3, E4F1, CHD4 and CHD7 to sites of DNA damage to a level comparable to that seen with expression of wild-type PARP1

Fig. 3 | HPF1 promotes chromatin relaxation at sites of DNA damage. a, Left: Confocal image sequences of the chromatin line area that is simultaneously damaged and photoconverted by irradiation at 405 nm in U2OS *WT*, *PARP1^{KO}*, *HPF1^{KO}* and *PARP1/HPF1* double-knockout cells expressing H2B-PAGFP. Scale bars, 2 µm. Right: Intensity profiles perpendicular to the irradiated lines (µm) at 0 s (black) and 120 s (red) after damage induction. Profile enlargement is due to the broadening of the photoconverted line consecutive to chromatin relaxation. **b**, Kinetics of chromatin relaxation in U2OS *WT*, *PARP1^{KO}*, *HPF1^{KO}* and *PARP1/HPF1* double-knockout cells after DNA damage induction by 405 nm laser irradiation. **c**, Chromatin relaxation in U2OS *WT*, *PARP1^{KO}*, *HPF1^{KO}* and *PARP1/HPF1* double-knockout cells at 120 s after irradiation. Data in **b** and **c** are representative of five independent replicates where data were collected from 13–16 cells per condition. **d**, Chromatin relaxation at 120 s after irradiation at 405 nm in *WT* and *PARP1^{KO}* cells expressing mCherry-PARP1 WT or PARP1 LW/AA. Data are representative of three independent replicates where data were collected from 12–16 cells per condition. ∅ denotes no plasmid expression. **e**, Chromatin relaxation at 120 s after irradiation at 405 nm in *WT* and *HPF1^{KO}* cells expressing mCherry-HPF1 D283A. Data are representative of three independent replicates where data were collected from 14–16 cells per condition. **f**,**g**, Quantification of the LacO array size in cells depleted for HPF1 or treated with PARPi after induction of bona fide DSBs by the FokI nuclease. **f**, γH2AX signals in U2OS 2-6-5 cells with DSBs at the LacO array induced by the expression of mCherry-LacI-FokI fusion. Inset shows magnified view of LacO array (**g**). The size of the LacO array, estimated from the mCherry-LacI-FokI staining and expressed in percentage of nuclear area determined based on DAPI staining. Data shows the mean ± s.e.m. LacO array size from 3–5 replicates where data were collected from 34–59 cells per condition. **h**, Kinetics of chromatin relaxation after irradiation at 405 nm in U2OS *WT* cells overexpressing mCherry-HPF1 or not. Data are representative of three independent replicates where data were collected from 20–21 cells per condition.

(Fig. 6g–i and Extended Data Fig. 7). Based on these different results, we propose that histone ADP-ribosylation-dependent chromatin unfolding triggered by the PARP1/HPF1 complex promotes the recruitment of the five studied repair factors ZNF384, ZMYM3, E4F1, CHD4 and CHD7.

HPF1 contributes to HR and NHEJ DNA repair efficiency

The DNA-binding factors ZNF384 and ZMYM3, whose recruitment to the sites of DNA damage are impaired in *HPF1*^{KO} cells (Fig. 6a–f), have been shown to act as scaffolding proteins stabilizing key components

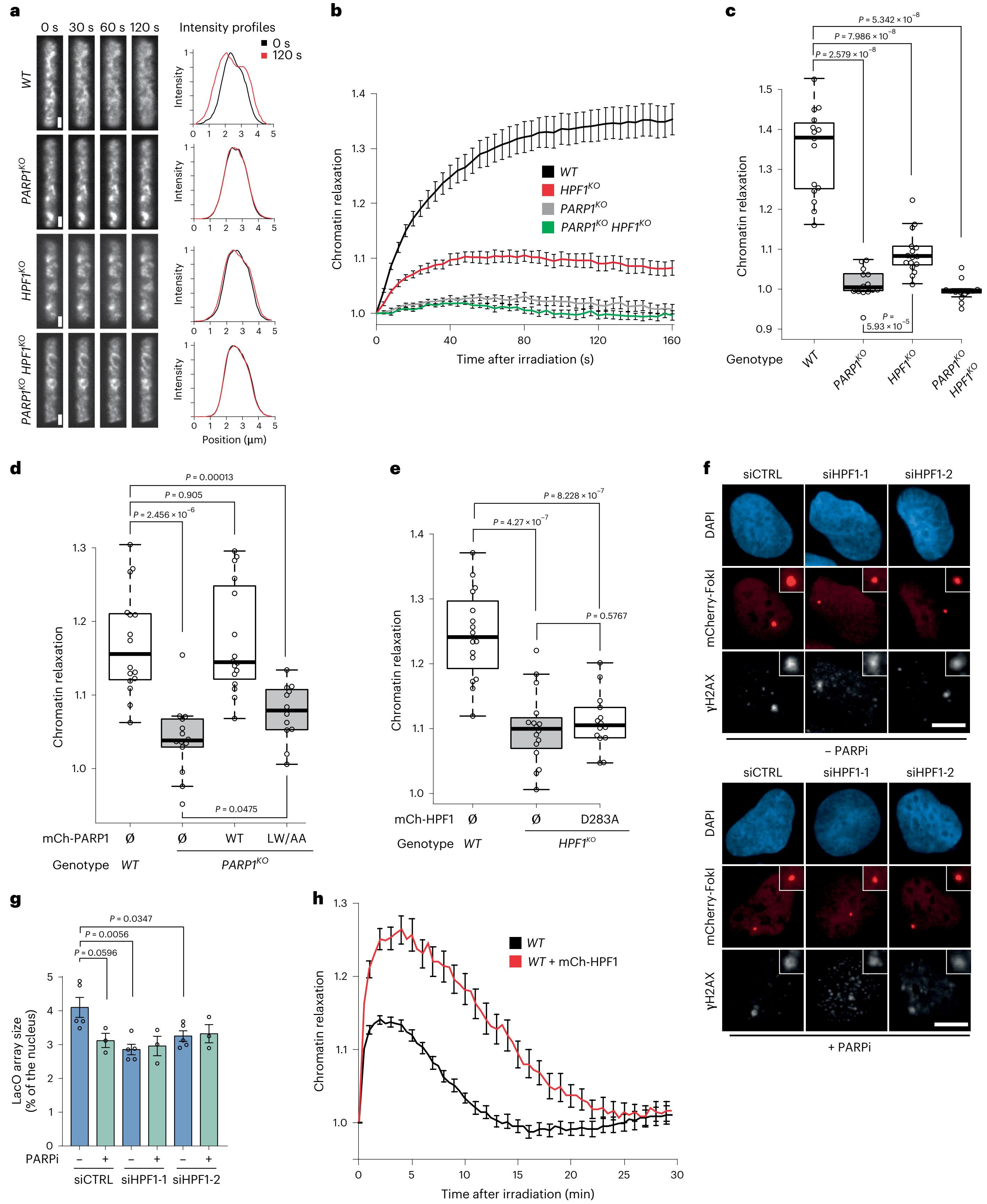

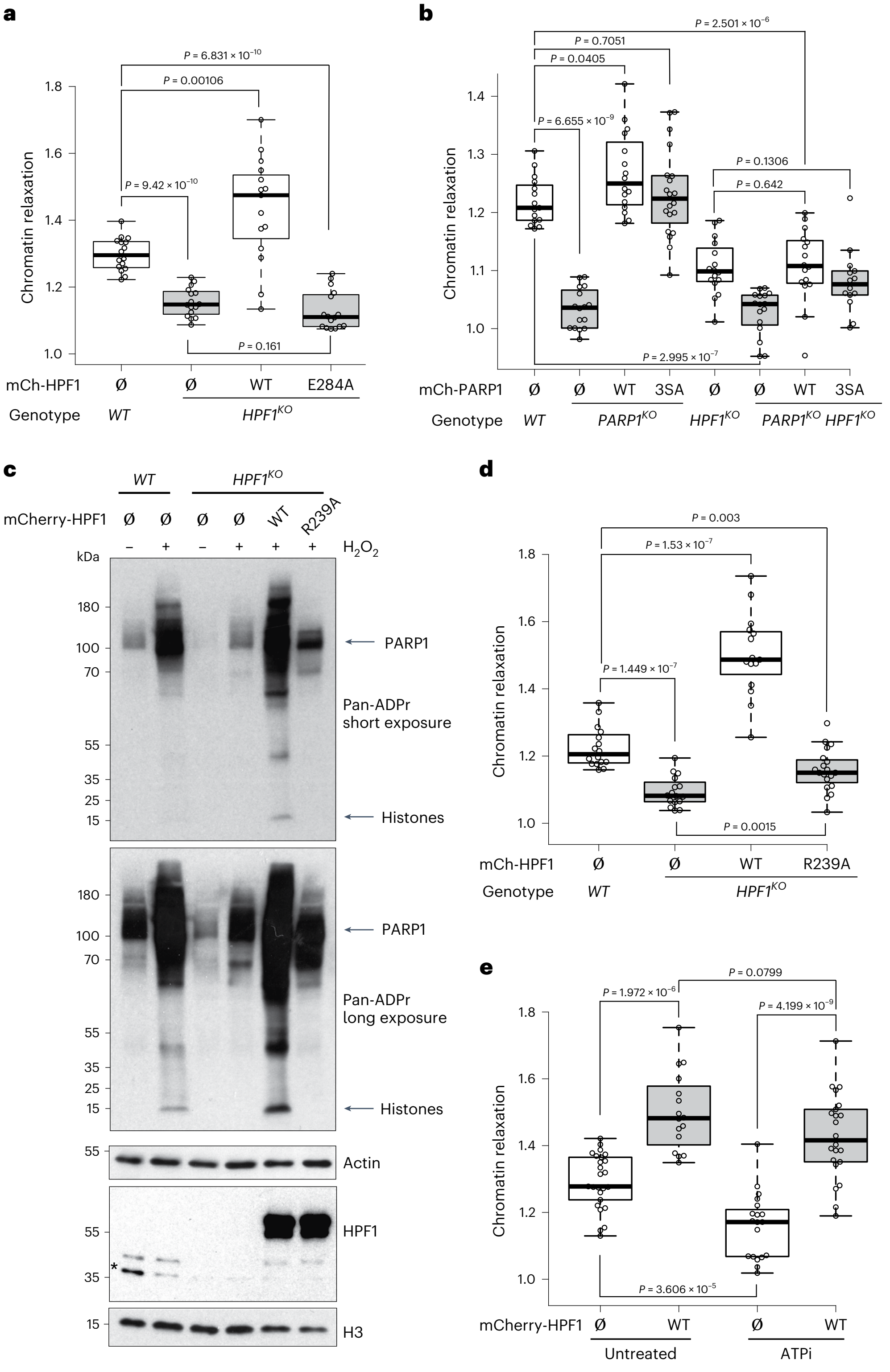

Fig. 4 | HPF1-dependent chromatin relaxation relies on *trans*-ADP-ribosylation of histones rather than PARP1 automodification. **a**, Chromatin relaxation at 120 s after irradiation at 405 nm in *WT* and *HPF1*^{KO} cells expressing mCherry-HPF1 E284A or not. Ø denotes no plasmid expression. Data in **a** are representative of three independent replicates where data were collected from 15–16 cells per condition. **b**, Chromatin relaxation at 120 s after irradiation at 405 nm in U2OS *WT*, *PARP1*^{KO}, *HPF1*^{KO} and *PARP1/HPF1* double-knockout cells. Cells are complemented with either mCherry-PARP1 WT or PARP1 3SA mutant. Data in **b** are representative of three independent replicates where data were collected from 15–20 cells per condition. **c**, Western blot displaying ADPr signals, stained with a pan-ADPr antibody, in *WT* cells and *HPF1*^{KO} cells expressing mCherry-tagged HPF1 WT or HPF1 R239A, and treated or not with H_2O_2. H3 and tubulin were used as loading controls. **d**, Chromatin relaxation at 120 s after irradiation at 405 nm in *WT* and *HPF1*^{KO} cells expressing mCherry-HPF1 R239A. Data in **d** are representative of three independent replicates where data were collected from 15–19 cells per condition. **e**, Chromatin relaxation at 120 s after irradiation at 405 nm in U2OS *WT* cells overexpressing mCherry-HPF1 and depleted or not for ATP (ATPi). Data in **e** are representative of three independent replicates where data were collected from 16–25 cells per condition.

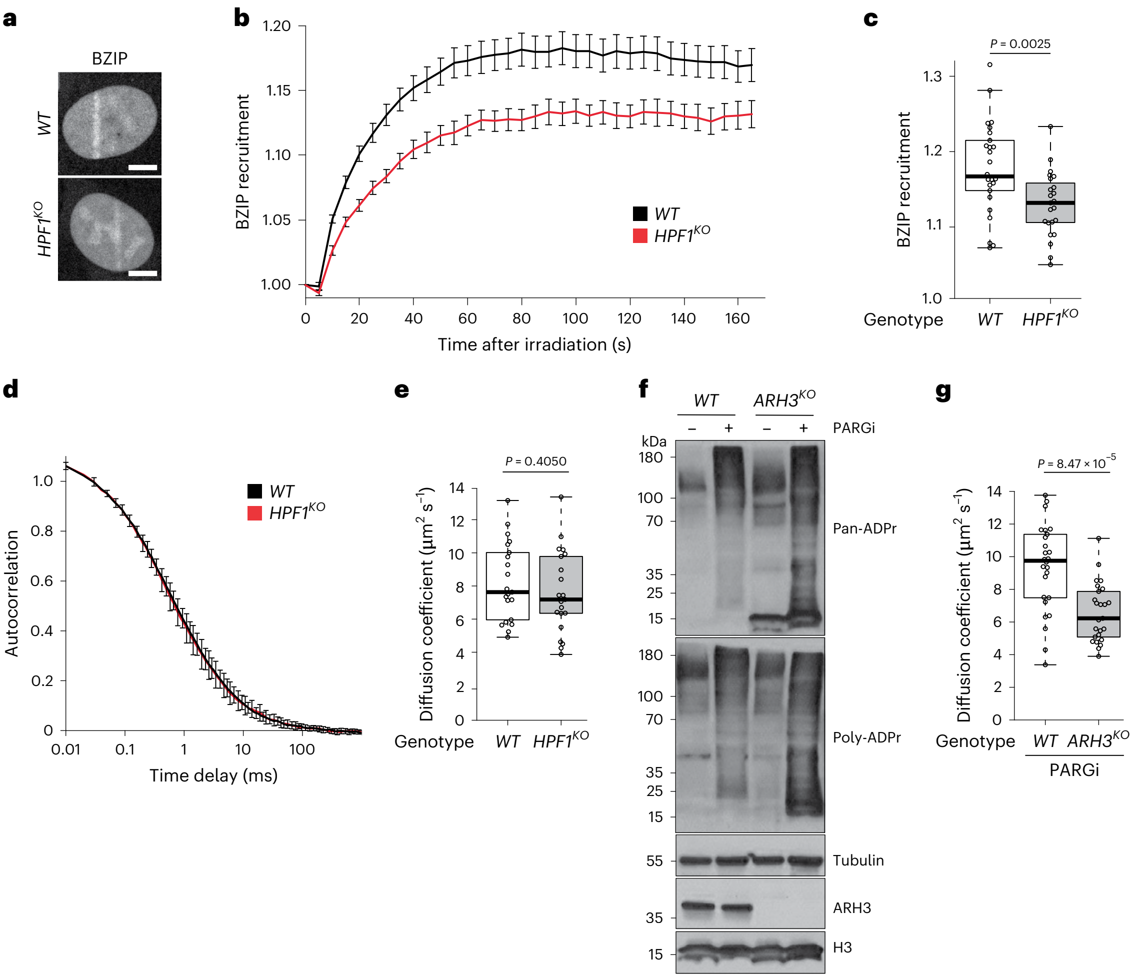

Fig. 5 | HPF1-dependent chromatin relaxation facilitates access to DNA in the vicinity of the DNA lesions. **a**–**c**, Representative confocal images (**a**), recruitment kinetics (**b**) and mean recruitment intensity at 120 s after irradiation (**c**) of GFP-BZIP at sites of DNA damage induced by 405 nm laser irradiation in U2OS *WT* and *HPF1^{KO}* cells. Confocal images are 120 s after irradiation. Scale bar, 5 µm. Recruitment kinetic curves show the mean ± s.e.m. Data in **b** and **c** are representative of three independent replicates where data were collected from 23–25 cells per condition. **d**, FCS autocorrelation curves of GFP-BZIP in U2OS *WT* and *HPF1^{KO}* cells. **e**, Diffusion coefficients estimated from the FCS curves of GFP-BZIP in U2OS *WT* and *HPF1^{KO}* cells. Data in **d** and **e** are representative of three independent replicates where data were collected from 21 cells per condition. **f**, Western blot displaying APDr signal, stained with pan-ADPr and poly-ADPr antibodies, in *WT* or *ARH3^{KO}* with or without 4 days of PARGi (25 µM) treatment. Tubulin and H3 are used as loading controls. **g**, Diffusion coefficients estimated from FCS acquisitions of GFP-BZIP in U2OS *WT* and *ARH3^{KO}* cells with 4 days of PARGi (25 uM) treatment. Data in **g** are representative of three independent replicates where data were collected from 25–26 cells per condition.

of the non-homologous end joining (NHEJ) and homologous recombination (HR) pathways at sites of damage, such as Ku70/Ku80 and XRCC4 for ZNF384 (ref. 28), and BRCA1 for ZMYM3 (ref. 29). We found that, along with the reduced accumulation of ZNF384 and ZMYM3 upon HPF1 depletion, the recruitment of both XRCC4 and BRCA1 to DNA lesions was impaired in *HPF1^{KO}* cells compared with *WT* cells (Fig. 7a–f). Therefore, by promoting the recruitment of early scaffolding factors, HPF1-dependent chromatin relaxation appears crucial for the later accumulation of core HR and NHEJ components.

We also studied the behavior of the core NHEJ factor APLF, whose recruitment to sites of damage is mainly triggered by its binding to ADPr moieties via dedicated PBZ motifs[31]. We found that APLF recruitment to laser-induced damage was reduced in *HPF1^{KO}* cells (Fig. 7g–i). Furthermore, we observed that the expression of PARP1 3SA, but not that of PARP1 LW/AA, is able to promote APLF recruitment similar to PARP1 WT (Fig. 7j–l). Therefore, our data suggest that the PBZ motifs of APLF preferentially recognize ADP-ribosylated histones as opposed to automodified PARP1 at sites of damage.

Finally, we assessed the contribution of HPF1 to efficient DNA repair. Previous reports have shown that HPF1-deficient cells are hypersensitive to the alkylating agent methyl methanesulfonate[8]. Here, we demonstrate that *HPF1^{KO}* cells were also hypersensitive to acute treatment with the topoisomerase inhibitors camptothecin and etoposide (Fig. 8a–d), highlighting a role of HPF1 in protecting cells from various genotoxic stressors. We also analyzed the effect of the expression of different PARP1 mutants on the hypersensitivity of *PARP1^{KO}* cells to continuous camptothecin treatment. PARP1 3SA, which led to the highest levels of histone ADP-ribosylation while being defective for automodification, provided greater protection from genotoxic stress than both the PARP1 LW/AA mutant and PARP1 WT (Fig. 8e,f and Extended Data Fig. 8a–c). These findings indicate that HPF1-dependent histone ADP-ribosylation, rather than PARP1 automodification, is important for efficient repair. Finally, using the well-established DR-GFP and EJ5-GFP reporter cell lines, we found that HPF1 knockdown impaired the efficiency of DSB repair by both HR and NHEJ (Fig. 8g,h and Extended Data Fig. 8d–h). In conclusion, by controlling the targets of ADP-ribosylation as well as

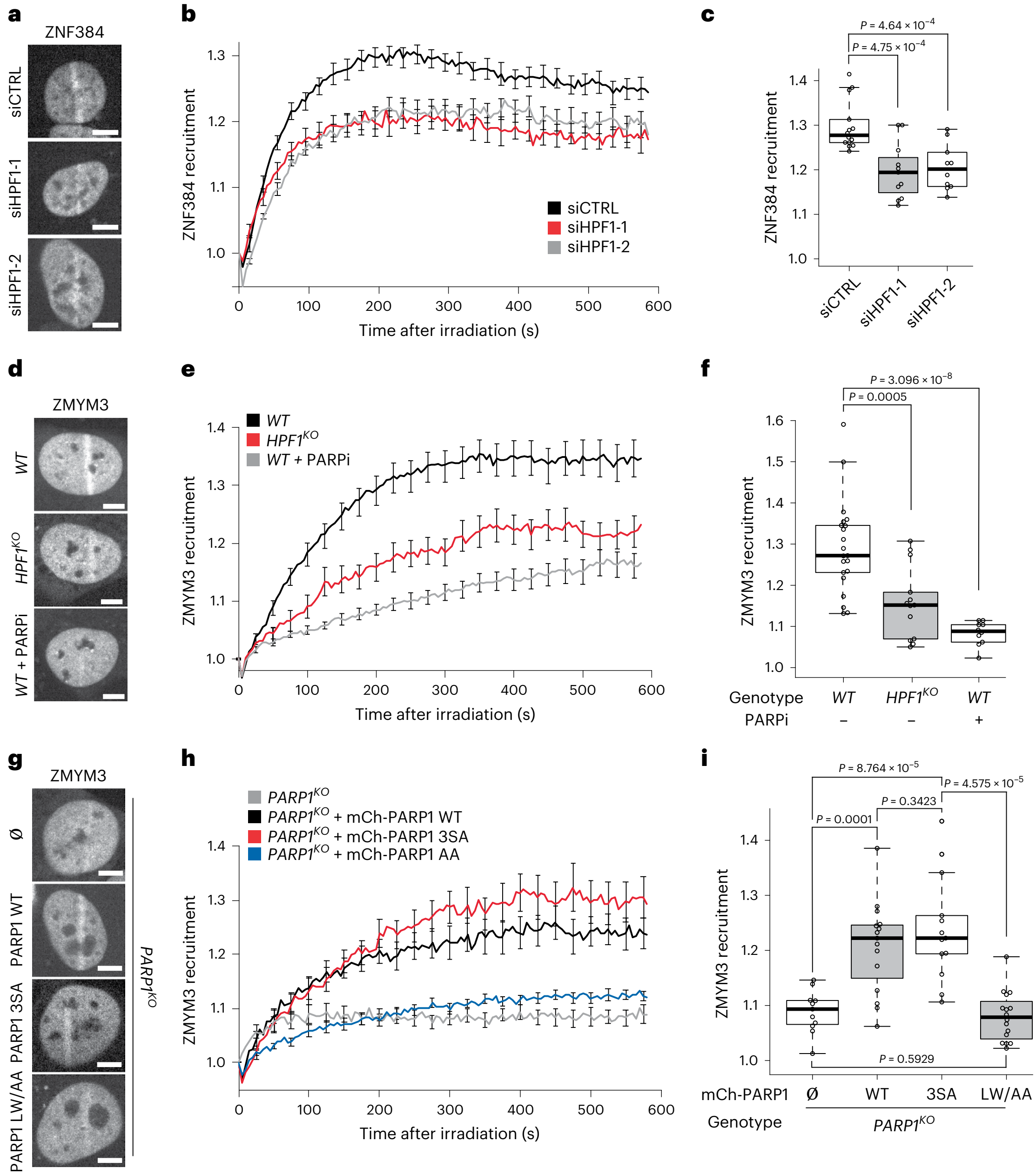

Fig. 6 | Increased access to DNA triggered by HPF1-dependent chromatin unfolding promotes the accumulation of DNA-binding repair factors at sites of DNA damage. **a**–**c**, Representative confocal images (**a**), recruitment kinetics (**b**) and mean recruitment intensity at 200 s after irradiation (**c**) of GFP-ZNF384 at sites of DNA damage induced by 405 nm laser irradiation in U2OS *ZNF384*^{KO} cells depleted of HPF1. Confocal images are 200 s after irradiation. Scale bar, 5 µm. Recruitment kinetic curves show the mean ± s.e.m. Data in **b** and **c** are representative of three independent replicates where data were collected from 10–14 cells per condition. **d**–**f**, Representative confocal images (**d**), recruitment kinetics (**e**) and mean recruitment intensity at 100 s after irradiation (**f**) of GFP-ZMYM3 at sites of DNA damage induced by 405 nm laser irradiation in U2OS *WT* and *HPF1*^{KO} cells treated or not with PARPi. Confocal images are 100 s after irradiation. Scale bar, 5 µm. Recruitment kinetic curves show the mean ± s.e.m. Data in **e** are representative of three independent replicates where data were collected from 10–21 cells per condition. **g**–**i**, Representative confocal images (**g**), recruitment kinetics (**h**) and mean recruitment intensity at 200 s after irradiation (**i**) of GFP-ZMYM3 at sites of DNA damage induced by 405 nm laser irradiation in U2OS *PARP1*^{KO} cells complemented or not with mCherry-PARP1 WT, PARP1 3SA or PARP1 LW/AA. Confocal images are 200 s after irradiation. Scale bar, 5 µm. Recruitment kinetic curves show the mean ± s.e.m. Data in **h** and **i** are representative of three independent replicates where data were collected from 11–16 cells per condition.

the chromatin packing state, HPF1 appears pivotal for the stabilization of the HR and NHEJ machineries at sites of damage and allowing efficient DNA repair.

Discussion

ADP-ribosylation is one of the earliest signaling pathways activated during the DDR[32]. It is well established that PARP1 is the central engine triggering this signaling pathway via its rapid recruitment to DNA lesions[2], but recent reports have demonstrated that this process also requires a steering wheel, the co-factor HPF1, to dictate the choice of the target proteins that will be ADP-ribosylated[9–11]. The loss of HPF1 does not suppress PARP1 activity but drastically reduces the number of ADP-ribosylation targets upon genotoxic stress and loosens the specificity for the serine residues[12]. In this report, we demonstrate

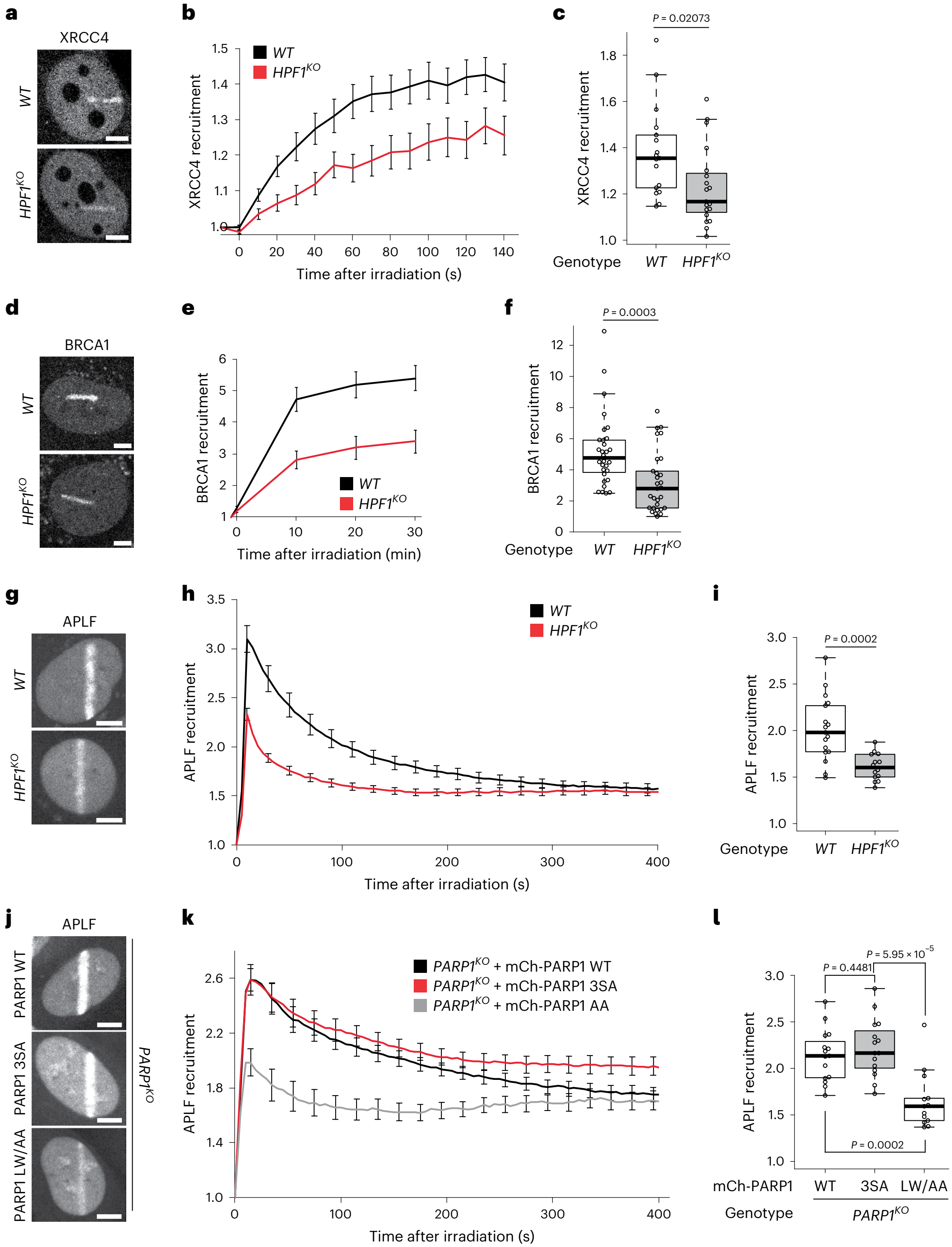

Fig. 7 | HPF1 controls the recruitment of HR and NHEJ factors at sites of DNA damage. a–**c**, Representative confocal images (**a**), recruitment kinetics (**b**) and mean recruitment intensity at 60 s after irradiation (**c**) of GFP-XRCC4 at sites of DNA damage induced by 800 nm laser irradiation in U2OS *WT* and *HPF1*^{KO} cells. Confocal images are 60 s after irradiation. Scale bar, 5 µm. Recruitment kinetic curves show the mean ± s.e.m. Data in **b** and **c** are representative of three independent replicates where data were collected from 17–19 cells per condition. **d**–**f**, Representative confocal images (**d**), recruitment kinetics (**e**) and mean intensity recruitment at 20 min after irradiation (**f**) of GFP-BRCA1 at sites of DNA damage induced by 800 nm laser irradiation in U2OS *WT* and *HPF1*^{KO} cells. Confocal images are 20 min after irradiation. Scale bar, 5 µm. Recruitment kinetic curves show the mean ± s.e.m. Data in **e** and **f** are representative of three independent replicates where data were collected from 29–31 cells per condition. **g**–**i**, Representative confocal images (**g**), recruitment kinetics (**h**) and mean recruitment intensity at 100 s after irradiation (**i**) of YFP-APLF at sites of DNA damage induced by 405 nm laser irradiation in U2OS *WT* and *HPF1*^{KO} cells. Confocal images are 100 s after irradiation. Scale bar, 5 µm. Recruitment kinetic curves show the mean ± s.e.m. Data in **h** and **i** are representative of three independent replicates where data were collected from 14–17 cells per condition. **j**–**l**, Representative confocal images (**j**), recruitment kinetics (**k**) and mean recruitment intensity at 100 s after irradiation (**l**) of YFP-APLF at sites of DNA damage induced by 405 nm laser irradiation in U2OS *PARP*^{KO} cells complemented with mCherry-PARP1 WT, PARP1 3SA or PARP1 LW/AA. Confocal images are 100 s after irradiation. Scale bar, 5 µm. Recruitment kinetic curves show the mean ± s.e.m. Data in **k** and **l** are representative of three independent replicates where data were collected from 13–15 cells per condition.

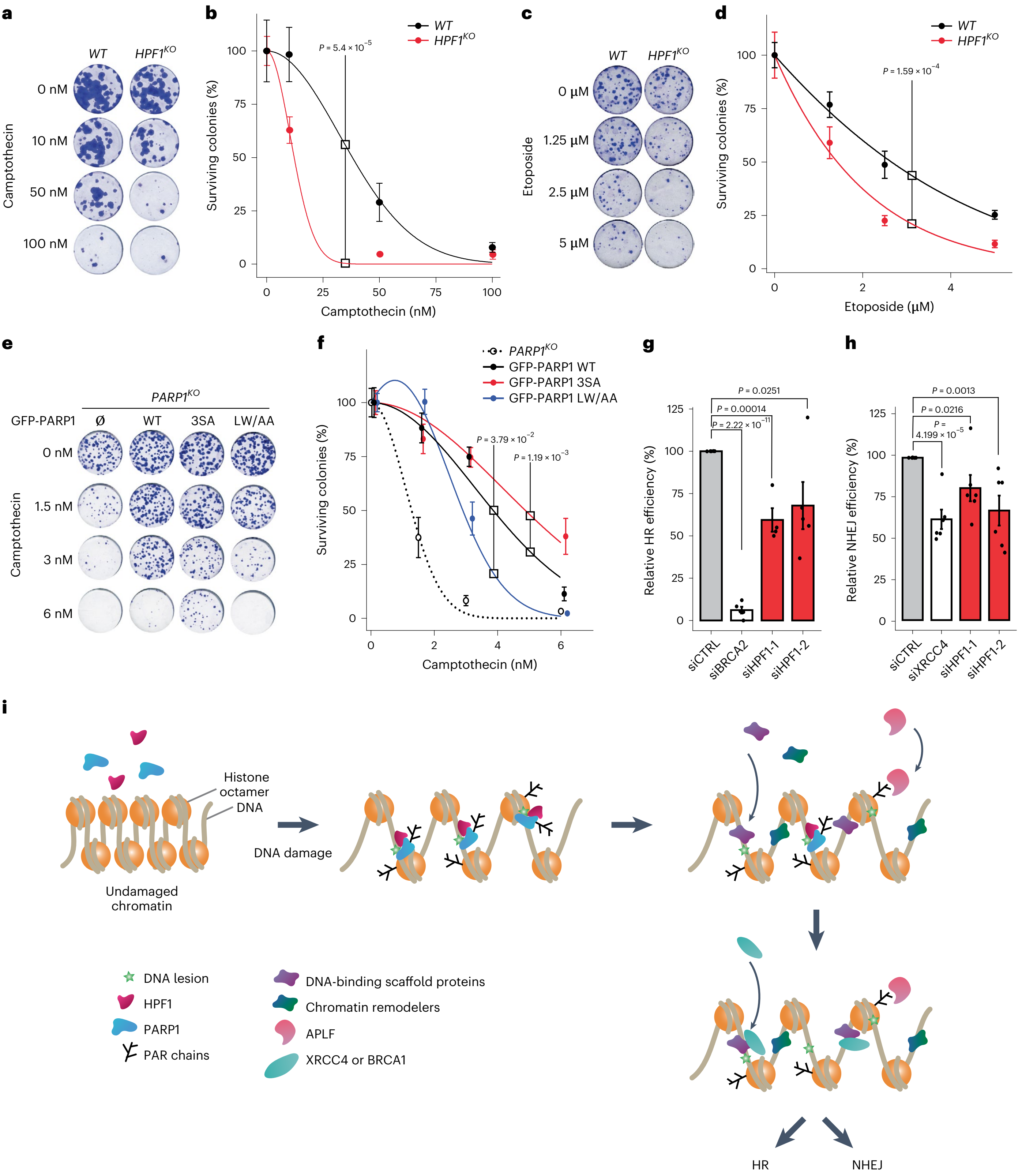

that, although the accumulation of HPF1 to sites of damage is triggered by its interaction with PARP1 (Fig. 1e), the two factors display different release speeds (Fig. 1b,c). The gradual increase of the HPF1/PARP1 ratio over time that we observed at sites of damage is in line with a prolonged ADP-ribosylation of the histones compared with the short-lived automodification of PARP1 (Fig. 1d). Since our live-cell data demonstrate that, in agreement with in vitro findings[13,16,33], HPF1 restricts the elongation of the ADPr chains (Fig. 2), this temporal evolution of the HPF1/PARP1 ratio could also support the notion of sustained signaling composed of short ADPr oligomers as opposed to the early burst of poly-ADP-ribosylation. Such a model is supported by recent reports demonstrating the prevalence of mono-ADPr or oligo-ADPr modifications compared with poly-ADPr chains in the DDR context[12,34]. Although further work will be needed to better understand

Fig. 8 | HPF1 contributes to efficient DNA repair. a,**b**, Representative images of clonogenic assay (**a**) and cell survival curves (**b**) for *WT* and *HPF1*^{KO} cells upon acute camptothecin treatment. Data are representative of two independent replicates. **c**,**d**, Representative images of clonogenic assay (**c**) and cell survival curves (**d**) for *WT* and *HPF1*^{KO} cells upon acute etoposide treatment. Data are representative of three independent replicates. **e**,**f**, Representative images of clonogenic assay (**e**) and cell survival curves (**f**) for *PARP1*^{KO} cells or *PARP1*^{KO} cells stably expressing GFP-tagged PARP1 WT, PARP1 3SA or PARP1 LW/AA with continuous camptothecin treatment. Data are representative of three independent replicates. **g**, Quantification of DR-GFP-positive U2OS cells transfected with the indicated siRNA and I-SceI expression vector. The mean ± s.e.m. of five independent experiments is shown. Data were normalized to siCTRL, which was set to 100%. **h**, Quantification of EJ5-GFP-positive U2OS cells transfected with the indicated siRNA and I-SceI expression vector. The mean ± s.e.m. of six independent experiments is shown. Data were normalized to siCTRL, which was set to 100%. **i**, Model for the role of HPF1 at sites of DNA damage. Upon damage, HPF1 interacts with PARP1 at sites of damage and promotes both PARP1 automodification and *trans*-ADP-ribosylation of histone. Histone ADP-ribosylation acts as a binding site for the repair factor APLF and triggers chromatin relaxation in the vicinity of a DNA lesion to promote the recruitment of DNA-binding repair factors that are scaffolding proteins for downstream repair factors. Together, these processes facilitate genome restoration by both HR and NHEJ.

the mechanisms underlying the slow release of HPF1 from the lesions, our work highlights that ADP-ribosylation signaling does not occur as a single early wave but rather can be decomposed into temporally distinct phases that differ in terms of targets and characteristics of the ADPr marks.

Although the role of ADPr moieties as a binding platform for repair factors has been studied extensively[35], less is known about the direct effect of these ADPr chains on the function of the proteins to which they are attached. While automodification of PARP1 is crucial for its timely mobilization from sites of damage[17,36], the direct effect of *trans*-ADP-ribosylation, in particular on histones, has not been elucidated. Here, we demonstrate that HPF1-dependent histone ADP-ribosylation is a major contributor to the transient unfolding of chromatin (Figs. 3 and 4), a process that promotes DNA accessibility in the vicinity of DNA lesions (Fig. 5). Seminal in vitro work found that the ADP-ribosylation of histones was sufficient to decondense purified chromatin fibers[37], a process that does not require histone eviction[38,39]. In line with these findings, we now show in living cells that the addition of ADPr onto histones is itself sufficient to promote chromatin unfolding without the need for active nucleosome disassembly (Fig. 4e). Nevertheless, several ATP-dependent remodelers have also been shown to contribute to early chromatin relaxation at sites of damage[24–26,40], including ALC1/CHD1L, which preferentially remodels ADP-ribosylated nucleosomes[41,42]. It will be important in the future to define whether these different modalities of chromatin remodeling are coordinated or work independently. These findings regarding the role of histone ADP-ribosylation in the regulation of the chromatin go beyond the context of the DDR. Indeed, we found that ADP-ribosylated chromatin displays an increased exposure of the DNA irrespective of the presence of DNA lesions (Fig. 5g). Therefore, any cellular process promoting histone ADP-ribosylation, in relation to either the DDR or transcriptional regulation[43], would lead to a chromatin conformation characterized by facilitated access to DNA.

Our work demonstrates the central role played by HPF1 in the initiation of the DNA repair process. Indeed, histone ADP-ribosylation triggered by the PARP1/HPF1 complex facilitates the recruitment of early repair factors both by serving as preferred binding sites such as for APLF, and by unfolding the chromatin to facilitate access to DNA for the several DNA-binding factors tested: ZNF384, ZMYM3, E4F1, CHD4 and CHD7 (Figs. 6, 7 and 8i and Extended Data Figs. 6 and 7). These different actors serve two main purposes at early stages of the DDR. First, the histone chaperone function of APLF[44] and the remodeling activities of CHD4, CHD7 and BRG1, which is recruited to sites of damage by E4F1, are probably required to establish a repair-competent chromatin architecture in the vicinity of DNA lesions[25,26,30]. Second, ZNF384 and ZMYM3 act as scaffolding factors to stabilize core members of the HR and NHEJ machineries, such as XRCC4 and BRCA1, at DNA lesions[28,29]. In conclusion, histone ADP-ribosylation triggered by the PARP1/HPF1 complex exerts its function prior to the repair pathway choice by facilitating the recruitment of early repair actors via different mechanisms, which ensures a rapid restoration of genome integrity (Fig. 8i).

Online content

Any methods, additional references, Nature Portfolio reporting summaries, source data, extended data, supplementary information, acknowledgements, peer review information; details of author contributions and competing interests; and statements of data and code availability are available at https://doi.org/10.1038/s41594-023-00977-x.

References

1. Kraus, W. L. & Hottiger, M. O. PARP-1 and gene regulation: progress and puzzles. *Mol. Aspects Med.* **34**, 1109–1123 (2013).
2. Chaudhuri, A. R. & Nussenzweig, A. The multifaceted roles of PARP1 in DNA repair and chromatin remodelling. *Nat. Rev. Mol. Cell Biol.* **18**, 610–621 (2017).
3. Eustermann, S. et al. Structural basis of detection and signaling of DNA single-strand breaks by human PARP-1. *Mol. Cell* **60**, 742–754 (2015).
4. Ali, A. A. E. et al. The zinc-finger domains of PARP1 cooperate to recognize DNA strand breaks. *Nat. Struct. Mol. Biol.* **19**, 685–692 (2012).
5. Langelier, M.-F., Planck, J. L., Roy, S. & Pascal, J. M. Structural basis for DNA damage–dependent poly(ADP-ribosyl)ation by human PARP-1. *Science* **336**, 728–732 (2012).
6. Leidecker, O. et al. Serine is a new target residue for endogenous ADP-ribosylation on histones. *Nat. Chem. Biol.* **12**, 998–1000 (2016).
7. Buch-Larsen, S. C. et al. Mapping physiological ADP-ribosylation using activated ion electron transfer dissociation. *Cell Rep.* **32**, 108176 (2020).
8. Gibbs-Seymour, I., Fontana, P., Rack, J. G. M. & Ahel, I. HPF1/C4orf27 Is a PARP-1-interacting protein that regulates PARP-1 ADP-ribosylation activity. *Mol. Cell* **62**, 432–442 (2016).
9. Suskiewicz, M. J. et al. HPF1 completes the PARP active site for DNA damage-induced ADP-ribosylation. *Nature* **579**, 598–602 (2020).
10. Palazzo, L. et al. Serine is the major residue for ADP-ribosylation upon DNA damage. *eLife* **7**, e34334 (2018).
11. Bonfiglio, J. J. et al. Serine ADP-ribosylation depends on HPF1. *Mol. Cell* **65**, 932–940.e6 (2017).
12. Hendriks, I. A. et al. The regulatory landscape of the human HPF1- and ARH3-dependent ADP-ribosylome. *Nat. Commun.* **12**, 5893 (2021).
13. Rudolph, J., Roberts, G., Muthurajan, U. M. & Luger, K. HPF1 and nucleosomes mediate a dramatic switch in activity of PARP1 from polymerase to hydrolase. *eLife* **10**, e65773 (2021).
14. Sun, F.-H. et al. HPF1 remodels the active site of PARP1 to enable the serine ADP-ribosylation of histones. *Nat. Commun.* **12**, 1028 (2021).
15. Mahadevan, J. et al. Q-FADD: a mechanistic approach for modeling the accumulation of proteins at sites of DNA damage. *Biophys. J.* **116**, 2224–2233 (2019).

16. Langelier, M.-F., Billur, R., Sverzhinsky, A., Black, B. E. & Pascal, J. M. HPF1 dynamically controls the PARP1/2 balance between initiating and elongating ADP-ribose modifications. *Nat. Commun.* **12**, 6675 (2021).
17. Prokhorova, E. et al. Serine-linked PARP1 auto-modification controls PARP inhibitor response. *Nat. Commun.* **12**, 4055 (2021).
18. Juhász, S. et al. The chromatin remodeler ALC1 underlies resistance to PARP inhibitor treatment. *Sci. Adv.* **6**, eabb8626 (2020).
19. Shao, Z. et al. Clinical PARP inhibitors do not abrogate PARP1 exchange at DNA damage sites in vivo. *Nucleic Acids Res.* **48**, 9694–9709 (2020).
20. Gibson, B. A., Conrad, L. B., Huang, D. & Kraus, W. L. Generation and characterization of recombinant antibody-like ADP-ribose binding proteins. *Biochemistry* **56**, 6305–6316 (2017).
21. Timinszky, G. et al. A macrodomain-containing histone rearranges chromatin upon sensing PARP1 activation. *Nat. Struct. Mol. Biol.* **16**, 923–929 (2009).
22. Wang, Z. et al. Recognition of the iso-ADP-ribose moiety in poly(ADP-ribose) by WWE domains suggests a general mechanism for poly(ADP-ribosyl)ation-dependent ubiquitination. *Genes Dev.* **26**, 235–240 (2012).
23. Smith, R. et al. Poly(ADP-ribose)-dependent chromatin unfolding facilitates the association of DNA-binding proteins with DNA at sites of damage. *Nucleic Acids Res.* **47**, 11250–11267 (2019).
24. Sellou, H. et al. The poly(ADP-ribose)-dependent chromatin remodeler Alc1 induces local chromatin relaxation upon DNA damage. *Mol. Biol. Cell* **27**, 3791–3799 (2016).
25. Rother, M. B. et al. CHD7 and 53BP1 regulate distinct pathways for the re-ligation of DNA double-strand breaks. *Nat. Commun.* **11**, 5775 (2020).
26. Smith, R., Sellou, H., Chapuis, C., Huet, S. & Timinszky, G. CHD3 and CHD4 recruitment and chromatin remodeling activity at DNA breaks is promoted by early poly(ADP-ribose)-dependent chromatin relaxation. *Nucleic Acids Res.* **46**, 6087–6098 (2018).
27. Prokhorova, E. et al. Unrestrained poly-ADP-ribosylation provides insights into chromatin regulation and human disease. *Mol. Cell* **81**, 2640–2655.e8 (2021).
28. Singh, J. K. et al. Zinc finger protein ZNF384 is an adaptor of Ku to DNA during classical non-homologous end-joining. *Nat. Commun.* **12**, 6560 (2021).
29. Leung, J. W. C. et al. ZMYM3 regulates BRCA1 localization at damaged chromatin to promote DNA repair. *Genes Dev.* **31**, 260–274 (2017).
30. Moison, C. et al. Zinc finger protein E4F1 cooperates with PARP-1 and BRG1 to promote DNA double-strand break repair. *Proc. Natl Acad. Sci. USA* **118**, e2019408118 (2021).
31. Grundy, G. J. et al. APLF promotes the assembly and activity of non-homologous end joining protein complexes. *EMBO J.* **32**, 112–125 (2013).
32. Liu, C., Vyas, A., Kassab, M. A., Singh, A. K. & Yu, X. The role of poly ADP-ribosylation in the first wave of DNA damage response. *Nucleic Acids Res.* **45**, 8129–8141 (2017).
33. Kurgina, T. A. et al. Dual function of HPF1 in the modulation of PARP1 and PARP2 activities. *Commun. Biol.* **4**, 1259 (2021).
34. Bonfiglio, J. J. et al. An HPF1/PARP1-based chemical biology strategy for exploring ADP-ribosylation. *Cell* **183**, 1086–1102.e23 (2020).
35. Barkauskaite, E., Jankevicius, G., Ladurner, A. G., Ahel, I. & Timinszky, G. The recognition and removal of cellular poly(ADP-ribose) signals. *FEBS J.* **280**, 3491–3507 (2013).
36. Murai, J. et al. Trapping of PARP1 and PARP2 by clinical PARP inhibitors. *Cancer Res.* **72**, 5588–5599 (2012).
37. Poirier, G. G., de Murcia, G., Jongstra-Bilen, J., Niedergang, C. & Mandel, P. Poly(ADP-ribosyl)ation of polynucleosomes causes relaxation of chromatin structure. *Proc. Natl Acad. Sci. USA* **79**, 3423–3427 (1982).
38. Hananya, N., Daley, S. K., Bagert, J. D. & Muir, T. W. Synthesis of ADP-ribosylated histones reveals site-specific impacts on chromatin structure and function. *J. Am. Chem. Soc.* **143**, 10847–10852 (2021).
39. de Murcia, G. et al. Modulation of chromatin superstructure induced by poly(ADP-ribose) synthesis and degradation. *J. Biol. Chem.* **261**, 7011–7017 (1986).
40. Luijsterburg, M. S. et al. PARP1 links CHD2-mediated chromatin expansion and H3.3 deposition to DNA repair by non-homologous end-joining. *Mol. Cell* **61**, 547–562 (2016).
41. Bacic, L. et al. Structure and dynamics of the chromatin remodeler ALC1 bound to a PARylated nucleosome. *eLife* **10**, e71420 (2021).
42. Mohapatra, J. et al. Serine ADP-ribosylation marks nucleosomes for ALC1-dependent chromatin remodeling. *eLife* **10**, e71502 (2021).
43. Tulin, A. & Spradling, A. Chromatin loosening by poly(ADP)-ribose polymerase (PARP) at *Drosophila* puff loci. *Science* **299**, 560–562 (2003).
44. Mehrotra, P. V. et al. DNA repair factor APLF is a histone chaperone. *Mol. Cell* **41**, 46–55 (2011).

Methods

Plasmids

pmEGFP-WWE, PATagRFP-H2B[24], pH2B-PAGFP[45], pGFP-CHD4[46], pGFP-CHD7[25], pPARP1-mCherry[21], pmCherry-PARP1 WT, pmCherry-PARP1 E988K[18], pLacI-GFP trap[26], pcDNA3.1(+) (Thermo Fisher), pmCherry-C1 (Takara Bio), peGFP-BZIP[23], pcDNA5-FRT-TO-puro-eGFP-ZNF384[28] and pYFP-APLF[44] were previously described. pCBASceI was a gift from M. Jasin (Addgene plasmid 26477[47]), pcDNA5/FRT/TO-FLAG-EGFP-BRCA1 was a gift from J. Morris[48], pDEST-GFP-ZMYM3 was a gift from K. Miller[29], and pEGFP-C1-FLAG-XRCC4 was a gift from S. Jackson (Addgene plasmid 46959[49]). PARP1 3SA (S499A/S507A/S519A) cDNA was amplified from pDEST-YFP-PARP1-3SA[17] and ligated into pmCherry-C1 between *Bgl*II and *Xma*I. pmCherry-PARP1 L1013A/W1014A was made using site-directed mutagenesis with primers listed in Supplementary Table 1. MacroH2A1.1 macrodomain cDNA was amplified from pcDNA3.1-YFP-macroH2A1.1 macrodomain[21] and ligated into pEGFP-C1 between *Bgl*II and *Eco*RI. cDNA of HPF1 WT, R239A, D283A and E284 were amplified from pDEST-YFP-HPF1 WT, R239A, D283A and E284[9], respectively, with primers listed in Supplementary Table 1, and ligated into pEGFP-C1 or pmCherry-C1 between *Bgl*II and *Bam*HI. E4F1 was amplified from MSCV-GFP-E4F1, a gift from G. Sauvageau[30], with primers listed in Supplementary Table 1, and ligated into pEGFP-C1 between *Kpn*I and *Bgl*II.

Cell culture

All cells used in this study were cultured in DMEM (Sigma) or RPMI supplemented with 10% FBS, 100 µg ml^{-1} penicillin and 100 U ml^{-1} streptomycin and maintained at 37 °C in a 5% CO$_2$ incubator.

U2OS *WT*, U2OS *PARP1^{KO}*, U2OS *HPF1^{KO}* and U2OS *PARP1^{KO} HPF1^{KO}* double-knockout cells were generated previously[8]. U2OS *ARH3^{KO}* [27], *CHD7^{KO}* [25], *ALC1^{KO}* [24] and *ZNF384^{KO}* [28] cells were generated previously. U2OS-2B2 were generated previously[50]. U2OS-DR and U2OS-EJ5 cells were a gift from J. Stark[51]. U2OS 2-6-5 cells were a gift from R. Greenberg[52]. U2OS Flp-In/T-Rex *PARP1^{KO}* cells that express YFP-PARP1 after doxycycline induction were described previously[17]. U2OS Flp-In/T-Rex *HPF1^{KO}* cells that express YFP-HPF1 after doxycycline were made as described previously[17]. To induce expression of YFP-PARP1 or YFP-HPF1, cells were incubated with 10 ng ml^{-1} or 5 ng ml^{-1} doxycycline, respectively, for 24 h to obtain expression levels similar to endogenous levels. To generate *PARP1^{KO}* cells stably expressing GFP-tagged PARP1 WT, 3SA (automodification mutant) or LW/AA (HPF1 interaction mutant), U2OS *PARP1^{KO}* cells were transfected with the appropriate EGFP-PARP1 expression plasmids. Cells were then selected using media supplemented with 500 µg ml^{-1} G418. Expression of PARP1 and ADPr response to DNA damage in stable cell lines were verified by western blot. All experiments presented in this work were performed on unsynchronized cells.

Live-cell microscopy

U2OS cells were seeded into an eight-well Imaging Chamber CG (Zell-Kontakt) and transfected 48–72 h prior to imaging using X-tremeGENE HP (Roche) according to the manufacturer's instructions. For Fig. 6a–c, *ZNF384^{KO}* cells were transfected with HPF1 short interfering RNA (siRNA) using Lipofectamine RNAiMAX (Thermo Fisher) by reverse transfection according to the manufacturer's instructions 72 h prior to imaging. *ZNF384^{KO}* cells were then transfected with GFP-ZNF384 and H2B-PaTagRFP 48 h prior to imaging. For cell sensitization prior to laser irradiation at 405 nm, growth medium was aspirated from the Lab-Tek and replaced with fresh medium containing 0.15–0.3 µg ml^{-1} Hoechst 33342 for 1 h at 37 °C. Immediately prior to imaging, growth medium was replaced with CO$_2$-independent imaging medium (phenol red-free Leibovitz's L-15 medium (Life Technologies) supplemented with 20% FBS, 2 mM glutamine, 100 µg ml^{-1} penicillin and 100 U ml^{-1} streptomycin). ATP depletion was achieved by bathing the cells for at least 30 min with PBS containing 10% FBS, 10 mM NaN$_3$ and 50 mM 2-deoxyglucose[53]. Recruitment and chromatin relaxation time courses after laser irradiation at 405 nm were completed on a Ti-E inverted microscope (Nikon) equipped with a CSU-X1 spinning-disk head (Yokogawa), a Plan Apo ×60/1.4 N.A. oil-immersion objective lens and a sCMOS ORCA-Flash4.0 camera. The fluorescence of EGFP/PAGFP and mCherry/PATagRFP were excited with lasers at 490 nm and 561 nm, respectively. For fluorescence detection, we used bandpass filters adapted to the fluorophore emission spectra. Laser microirradiation and local photoactivation at 405 nm of Hoechst presensitized cells was performed along a 16-µm line through the nucleus using a single-point scanning head (iLas2, Roper Scientific) coupled to the epifluorescence backboard of the microscope. To ensure reproducibility, we measured laser power at 405 nm at the beginning of each experiment and set it to 125 µW at the sample level. Recruitment and chromatin relaxation time courses after laser irradiation at 800 nm were completed on a Zeiss LSM 880 confocal setup equipped with a C-Apo ×40/1.2 N.A. water-immersion objective. The pinhole was set to 1 Airy unit, and fluorescence detection was performed on a GaAsP detector array. The fluorescence of GFP/PAGFP was excited at 488 nm and detected within a window ranging from 500 nm to 550 nm. The fluorescence of mCherry/PATagRFP was excited at 561 nm and detected within a window ranging from 580 nm to 650 nm. The pixel size was set to 80 nm. Laser intensities and detector gains were chosen to avoid detector saturation, and the acquisition settings were kept constant within the course of a given experiment. Nuclei of non-sensitized cells were irradiated within a region of interest of 100-pixel width and 10-pixel height with a Ti:sapphire femtosecond infrared laser (Mai Tai HP, Spectra-Physics) with emission wavelength set to 800 nm. For all live-cell imaging experiments, cells were maintained at 37 °C with a heating chamber. Protein recruitment was quantified using a custom-made MATLAB (MathWorks) routine that measures the mean intensity within the damaged region (I_d) as determined by the segmentation of the photoactivated H2B signal, the mean nuclear fluorescence (I_n) and the mean background signal outside of the cell (I_{bg}). Protein accumulation at sites of damage (A_d) was then calculated as

$$A_d = \frac{I_d - I_{bg}}{I_n - I_{bg}}$$

The intensity within the microirradiated area was then normalized to the intensity prior to damage induction.

Chromatin relaxation was determined using a custom MATLAB routine that measures changes in the thickness of the photoconverted H2B line relative to its value immediately after damage induction[24].

The PAR3H assay (Extended Data Fig. 2i) has been previously described[26]. In brief, U2OS-2B2[50] cells containing the LacO array were transfected with GFP-macrodomain of macroH2A1.1, LacI-GFP trap, and mCherry-tagged PARP1 WT, PARP1 E988K or PARP1 3SA. Cells sensitized with Hoechst 33342 were irradiated away from the LacO array with 405 nm light to induce DNA damage as described above. Irrespective of its ADP-ribosylation status, PARP1 does not remain stably bound to DNA lesions but can quickly dissociate from this region and diffuse within the nucleus[18,19]. Therefore, the amount of accumulation of mCherry-tagged PARP1 at the LacO array due to interaction with the tethered macrodomain can then be used as a proxy to assess the level of ADP-ribosylation of the different PARP1 mutants. The mCherry intensity at the LacO array (A_{lo}) was quantified with the following equation, where I_o is the intensity of the LacO array, I_n is the mCherry signal in the nucleoplasm devoid of the LacO array and I_{bg} is the intensity of the background:

$$A_{lo} = \frac{I_o - I_{bg}}{I_n - I_{bg}}$$

The intensity within the LacO array was then normalized to the intensity prior to damage induction.

Fluorescence correlation spectroscopy

FCS experiments were performed on a Zeiss LSM 880 confocal setup equipped with a C-Apo ×40/1.2 N.A. water-immersion objective. GFP fluorescence was excited with a 488 nm laser, and single emitted photons at wavelength ranging between 500 nm and 550 nm were detected and counted on the GaAsP spectral detector. The laser power used for FCS measurements was adjusted to minimize photobleaching. Each FCS acquisition lasted 20 s to reduce the noise in the autocorrelation curves. Cells were maintained at 37 °C with a heating chamber. Raw photon traces obtained for GFP-tagged DNA-binding domains were detrended for slow fluctuations using Fluctuation Analyzer 4G software[54]. Autocorrelation curves were fitted with the following effective diffusion model:

$$G(t) = \frac{1}{N}\left(1 + t\frac{4D}{\omega^2}\right)^{-1}\left(1 + t\frac{4D}{(s\omega)^2}\right)^{-1/2}$$

where N is the number of tagged molecules in the focal volume, D is the effective diffusion coefficient, ω is the radial radius of the focal volume and s is the shape factor. N and D are fitted parameters, whereas ω and s are fixed and set to 160 nm and 6, respectively.

Characterization of the chromatin conformation

To assess chromatin compaction state, we estimated the fluorescence contrast on images of nuclei stained with Hoechst, using the plug-in GLCM_Texture written by J.E. Cabrera. The contrast is one of the Haralick features[55] and measures the mean squared intensity difference between pixels separated by a given distance d set to 7 pixels. As the measured contrast was independent of the cardinal directions, this parameter was only calculated along the east direction. The contrast estimated for each nucleus was the average of the values measured for three regions of 20 pixels × 20 pixels randomly chosen within this nucleus, ensuring that these regions do not overlap with the nucleus border or the nucleoli.

DSB reporter assay

U2OS 2-6-5 cells stably expressing ER-mCherry-LacR-FokI-DD41[52] were seeded on 18 mm coverslips and after 24 h were transfected with siRNAs using RNAiMAX (Invitrogen). Forty-eight hours after transfection, cells were treated for 1 h with 10 µM PARP inhibitor olaparib (Selleck Chemicals), followed by 4 h of treatment with 0.5 µM Shield-1 (Clontech Laboratories UK Ltd) and 1 µM 4-hydroxytamoxifen (4-OHT, Sigma-Aldrich) to induce DSBs. Subsequently, cells were fixed in 2% paraformaldehyde and permeabilized in 0.5% Triton X-100. Primary antibodies rabbit anti-PAR (Merck) and mouse anti-γH2AX (Millipore clone JBW301) were used to stain selected proteins and were detected with secondary antibodies anti-rabbit coupled to Alexa Fluor 488 (Invitrogen) and anti-mouse coupled to Alexa Fluor 647 (Invitrogen). Images were acquired on a Zeiss Axio Imager M2 or D2 widefield fluorescence microscope equipped with ×40, ×63 and ×100 Plan Apo (1.4 N.A.) oil-immersion objectives (Zeiss), an HXP 120 metal–halide lamp used for excitation and the following filters: DAPI (excitation filter (ExF), 350/50 nm; dichroic mirror (DM), 400 nm; emission filter (EmF), 460/50 nm), GFP/Alexa Fluor 488 (ExF, 470/40 nm; DM, 495 nm; EmF, 525/50 nm), mCherry (ExF, 560/40 nm; DM, 585 nm; EmF, 630/75 nm), Alexa Fluor 555 (ExF, 545/25 nm; DM, 565 nm; EmF, 605/70 nm) and Alexa Fluor 647 (ExF, 640/30 nm; DM, 660 nm; EmF, 690/50 nm). Images were recorded using ZEN 2012 software and analyzed in ImageJ. The array coordinates were determined based on the mCherry-FokI signal. The array size was quantified as a percentage of the nucleus size, which was determined based on 4,6-diamidino-2-phenylindole (DAPI) staining. The intensity of the ADPr signal was quantified at the array.

Proximity ligation assay

U2OS Flp-In/T-REx cells knocked out for HPF1 or PARP1 were seeded on 12 mm coverslips with 5 ng ml^{-1} or 10 ng ml^{-1} doxycycline to induce expression of YFP-HPF1 or YFP-PARP1, respectively. After 24 h, cells were irradiated with 2 Gy of ionizing radiation to induce DSBs. One hour after ionizing radiation, cells were fixed in 2% paraformaldehyde and permeabilized in 0.5% Triton X-100. Primary antibodies rabbit anti-GFP (Abcam, ab290) and mouse anti-γH2AX (Millipore clone JBW301) were used to stain selected proteins. Proximity ligation assay (PLA) was performed with Duolink In Situ PLA Probe Anti-Mouse Plus (Sigma) and Anti-Rabbit Minus (Sigma), and with Duolink In Situ Detection Reagents Orange (Sigma) according to the manufacturer's instructions. Finally, secondary antibodies anti-rabbit coupled to Alexa Fluor 488 (Invitrogen) and anti-mouse coupled to Alexa Fluor 647 (Invitrogen) were used to stain selected proteins in immunofluorescence. Images were acquired on a Zeiss Axio Imager M2 or D2 widefield fluorescence microscope equipped with ×40, ×63 and ×100 Plan Apo (1.4 N.A.) oil-immersion objectives (Zeiss), an HXP 120 metal–halide lamp used for excitation and the following filters: DAPI (ExF, 350/50 nm; DM, 400 nm; EmF, 460/50 nm), GFP/Alexa Fluor 488 (ExF, 470/40 nm; DM, 495 nm; EmF, 525/50 nm), mCherry (ExF, 560/40 nm; DM, 585 nm; EmF, 630/75 nm), Alexa Fluor 555 (ExF, 545/25 nm; DM, 565 nm; EmF, 605/70 nm) and Alexa Fluor 647 (ExF, 640/30 nm; DM, 660 nm; EmF, 690/50 nm). Images were recorded using ZEN 2012 software, and the number of PLA foci per cell was analyzed in ImageJ.

DNA repair assay

U2OS-DR and U2OS-EJ5 cells containing a stably integrated cassette of either the DR-GFP or EJ5-GFP reporter were used to measure the repair of I-SceI-induced DSBs by HR or by NHEJ, respectively[51]. In brief, cells were transfected with siRNA for 48 h prior to co-transfection with an mCherry expression vector and the I-SceI expression vector. The percentage of GFP-positive cells among the mCherry-positive cells was determined 48 h after I-SceI transfection using an LSRFortessa X-20 (BD Biosciences) with BD FACSDiva v8.0.1 software. Quantifications were performed with FACSDiva (BD Biosciences). siRNAs used in this study are listed in Supplementary Table 2.

Chromatin fractionation

U2OS *WT* cells seeded in 10-cm dishes were treated with 2 mM H_2O_2 diluted in cell culture media for 10 min. The media were then replaced with fresh cell culture media and incubated for 20 min, 25 min or 30 min. Cells were collected by trypsinisation and pelleted by centrifugation at 500*g* for 5 min. The cells were washed by suspending the cell pellet with ice-cold PBS. Chromatin fractionation was completed using the Subcellular Protein Fractionation kit according to the manufacturer's instructions (Thermo Fisher). Western blotting was used to visualize HPF1 and PARP1 in soluble and chromatin-bound fractions. H2B was used as a loading control to show effective fractionation of samples.

Immunofluorescence

Cells were seeded into an eight-well Imaging Chamber CG. Cells were either irradiated with 405 nm microirradiation (Extended Data Fig. 1a) or treated with siRNA (Extended Data Fig. 6a) as described above. Cells were washed once with PBS before being fixed with 4% paraformaldehyde for 15 min at 20 °C. Cells were then permeabilized with 0.1% Triton X-100 in PBS for 10 min at 20 °C, followed by blocking DMEM supplemented with 10% FBS for 1 h. Cells were incubated with primary antibody diluted in blocking buffer for 2 h at 20 °C. After being washed three times with PBS, cells were incubated with secondary antibody labeled with Alexa Fluor 647 diluted in blocking buffer for 1 h at 20 °C. Secondary antibody was removed, and cells were washed three times with PBS.

Western blotting

For whole-cell extract, cells were lysed on Triton-X buffer (1% Triton X-100, 100 mM NaCl, 50 mM Tris-HCl, pH 8.0, 5 mM $MgCl_2$, 0.1%

Benzonase (Sigma-Aldrich), 1× protease inhibitor (Roche)) on an orbital rotator for 30 min at 4 °C. Samples were centrifuged at 20,000*g* for 15 min, and supernatant was collected. Protein samples were quantified using Bradford (Bio-Rad), and equal amounts of protein were loaded on gels for SDS–PAGE prior to immunoblotting. Antibodies used in this study are listed in Supplementary Table 3. For DNA damage induction, cells were incubated in serum-free media prior to treatment with 2 mM H_2O_2 for 10 min. During cell lysis, Triton-X buffer was supplemented further with 2 µM olaparib (Selleck Chemicals) and 2 µM PARG inhibitor PDD00017273 (Sigma-Aldrich). For the H_2O_2 time course shown in Fig. 1d, media were removed from the cells and replaced with fresh cell culture media supplemented with 2 mM H_2O_2 for the indicated time. At the time of collection, the cells were washed twice in PBS before denaturing lysis buffer (4% SDS, 50 mM Tris-HCl, pH 7.4, 100 mM NaCl, 4 mM $MgCl_2$, 5 U Benzonase) was added directly to the cell culture dish. Cells were collected by scraping with a cell scraper and were sonicated for 1 min at 20 °C (20% power and 30% pulse). Total protein concentration was estimated by measuring absorbance at 280 nm on a NanoDrop (A280 setting), and samples were equalized accordingly. Samples were boiled in 4% Laemmli buffer for 5 min at 95 °C prior to western blotting. Full western blot panels are included in the Source Data files.

Clonogenic survival assay

U2OS *WT*, *HPF1*^{KO}, *PARP1*^{KO} and U2OS *PARP1*^{KO} cells stably expressing GFP-PARP1 WT, PARP1 3SA or PARP1 LW/AA were seeded in six-well plates 24 h before treatment with DNA-damaging agents. For acute DNA damage induction, cells were treated for 1 h with etoposide (0–5 µM) (Sigma-Aldrich) or camptothecin (0–100 nM) (Thermo Fisher Scientific) in cell culture media. The drug-containing media was aspirated, and cells were washed once with PBS and replenished with fresh cell culture media. Cells were then incubated for 10 days to allow colony formation. For continuous camptothecin treatment, cells were incubated in media containing camptothecin (0–6 nM) for 10 days to allow colony formation. Surviving colonies were washed with PBS three times and fixed and stained with a 16% paraformaldehyde (Electron Microscopy Sciences) / 5% ethanol solution containing crystal violet (Sigma-Aldrich). Colonies from each well were counted using a FIJI macro. Colonies with an area less than 0.067 mm^2 were discarded, and the subsequent fraction of surviving cells was normalized to untreated cases. For each condition, the replicate with a *Z* score higher than 1 for colony count was discarded. Dose–response curves were analyzed with GraphPad Prism v9.4 software. A linear quadratic survival model was fitted using the formula $Y = 100 \times e^{-(AX+BX^2)}$, where Y is the percentage of cells surviving, X is the drug dose, A is the coefficient for linear killing and B is the coefficient for quadratic killing. Statistics were performed using one-way analysis of variance (ANOVA) on the curve fittings.

Statistics and reproducibility

Data analysis and visualization were performed using R software (https://www.R-project.org). The box plot limits correspond to the 25th and 75th percentiles, and the bold line indicates the median value. The whiskers extend 1.5 times the interquartile range. The time-lapse curves are the mean ± s.e.m. of at least 15 cells per condition from a characteristic experiment among at least three independent repeats. The histograms show the mean ± s.e.m. of the independent experiments indicated in the figure legends. Unless stated otherwise, *P* values were calculated using an unpaired two-sided Student's *t*-test, assuming unequal variances. Western blots were completed a minimum of three times with a representative experiment presented in the figures.

Reporting summary

Further information on research design is available in the Nature Portfolio Reporting Summary linked to this article.

Data availability

The data sets generated and analyzed during the current study are not publicly available, as the large amount of imaging data could not be uploaded to a repository, but are available from the corresponding author upon request. Source data are provided with this paper.

Code availability

The MATLAB codes used in this work are available at https://github.com/sehuet/Smith-Zentout-image-processing.

References

45. Beaudouin, J., Mora-Bermúdez, F., Klee, T., Daigle, N. & Ellenberg, J. Dissecting the contribution of diffusion and interactions to the mobility of nuclear proteins. *Biophys. J.* **90**, 1878–1894 (2006).
46. Polo, S. E., Kaidi, A., Baskcomb, L., Galanty, Y. & Jackson, S. P. Regulation of DNA-damage responses and cell-cycle progression by the chromatin remodelling factor CHD4. *EMBO J.* **29**, 3130–3139 (2010).
47. Richardson, C., Moynahan, M. E. & Jasin, M. Double-strand break repair by interchromosomal recombination: suppression of chromosomal translocations. *Genes Dev.* **12**, 3831–3842 (1998).
48. Densham, R. M. et al. Human BRCA1–BARD1 ubiquitin ligase activity counteracts chromatin barriers to DNA resection. *Nat. Struct. Mol. Biol.* **23**, 647–655 (2016).
49. Britton, S., Coates, J. & Jackson, S. P. A new method for high-resolution imaging of Ku foci to decipher mechanisms of DNA double-strand break repair. *J. Cell Biol.* **202**, 579–595 (2013).
50. Czarna, A. et al. Structures of *Drosophila* cryptochrome and mouse cryptochrome1 provide insight into circadian function. *Cell* **153**, 1394–1405 (2013).
51. Gunn, A. & Stark, J. M. I-SceI-based assays to examine distinct repair outcomes of mammalian chromosomal double strand breaks. *Methods Mol. Biol.* **920**, 379–391 (2012).
52. Tang, J. et al. Acetylation limits 53BP1 association with damaged chromatin to promote homologous recombination. *Nat. Struct. Mol. Biol.* **20**, 317–325 (2013).
53. Platani, M., Goldberg, I., Lamond, A. I. & Swedlow, J. R. Cajal body dynamics and association with chromatin are ATP-dependent. *Nat. Cell Biol.* **4**, 502–508 (2002).
54. Wachsmuth, M. et al. High-throughput fluorescence correlation spectroscopy enables analysis of proteome dynamics in living cells. *Nat. Biotechnol.* **33**, 384–389 (2015).
55. Haralick, R. M., Shanmugam, K. & Dinstein, I. Textural features for image classification. *IEEE Trans. Syst. Man Cybern.* **SMC-3**, 610–621 (1973).

Acknowledgements

We thank the Microscopy-Rennes Imaging Center (BIOSIT, Université Rennes 1), a member of the national infrastructure France-BioImaging supported by the French National Research Agency (ANR-10-INBS-04), for providing access to the imaging setups, as well as S. Dutertre and X. Pinson for technical assistance on the microscopes. We also thank the Cytométrie en flux et tri cellulaire (BIOSIT, Université Rennes 1), specifically L. Deleurme and A. Aimé for technical assistance with flow cytometry. We also thank M. Suskiewicz for thoughtful discussions and generously sharing the HPF1 plasmid DNA. For this work, S.H.'s group received financial support from the Agence Nationale de la Recherche (PRC-2018 REPAIRCHROM), the Institut National du Cancer (PLBIO-2019) and the Institut Universitaire de France. R.S. is supported by the Fondation ARC pour la recherche sur le cancer (PDF20181208405). The work in G.T.'s laboratory was supported by the Hungarian Academy of Sciences (LP2017-11/2017) and the National Research Development and Innovation Office (K128239). The work in I.A.'s laboratory is supported by the Wellcome Trust (210634 and

223107), Biotechnology and Biological Sciences Research Council (BB/R007195/1), Ovarian Cancer Research Alliance (813369) and Cancer Research United Kingdom (C35050/A22284). H.v.A.'s laboratory is financially supported by a NWO-VICI grant (VI.C.182.052) from the Dutch Research Council (NWO).

Author contributions

R.S., G.T. and S.H. conceived the project with input from all authors. R.S., S.Z. and S.H. performed live-cell imaging and analyzed the imaging data. R.S., S.Z. and A.M performed ADPr western blots. N.B. performed colony formation assays. S.Z. performed the DNA repair assay and generated *PARP*^{KO} stable cell lines. C.C. and R.S. generated DNA constructs. F.F.Z. and I.A. generated U2OS Flp-In/T-REx *HPF1*^{KO} cells. M.R. and H.v.A. performed PLA and FokI assays. R.S., G.T. and S.H. wrote the paper with input from all authors.

Competing interests

The authors declare no competing interests.

Additional information

Extended data is available for this paper at https://doi.org/10.1038/s41594-023-00977-x.

Supplementary information The online version contains supplementary material available at https://doi.org/10.1038/s41594-023-00977-x.

Correspondence and requests for materials should be addressed to Rebecca Smith, Gyula Timinszky or Sébastien Huet.

Peer review information *Nature Structural & Molecular Biology* thanks Karolin Luger, Kumar Somyajit and the other, anonymous, reviewer(s) for their contribution to the peer review of this work. Primary Handling Editors: Beth Moorefield and Carolina Perdigoto, in collaboration with the *Nature Structural & Molecular Biology* team.

Reprints and permissions information is available at www.nature.com/reprints.

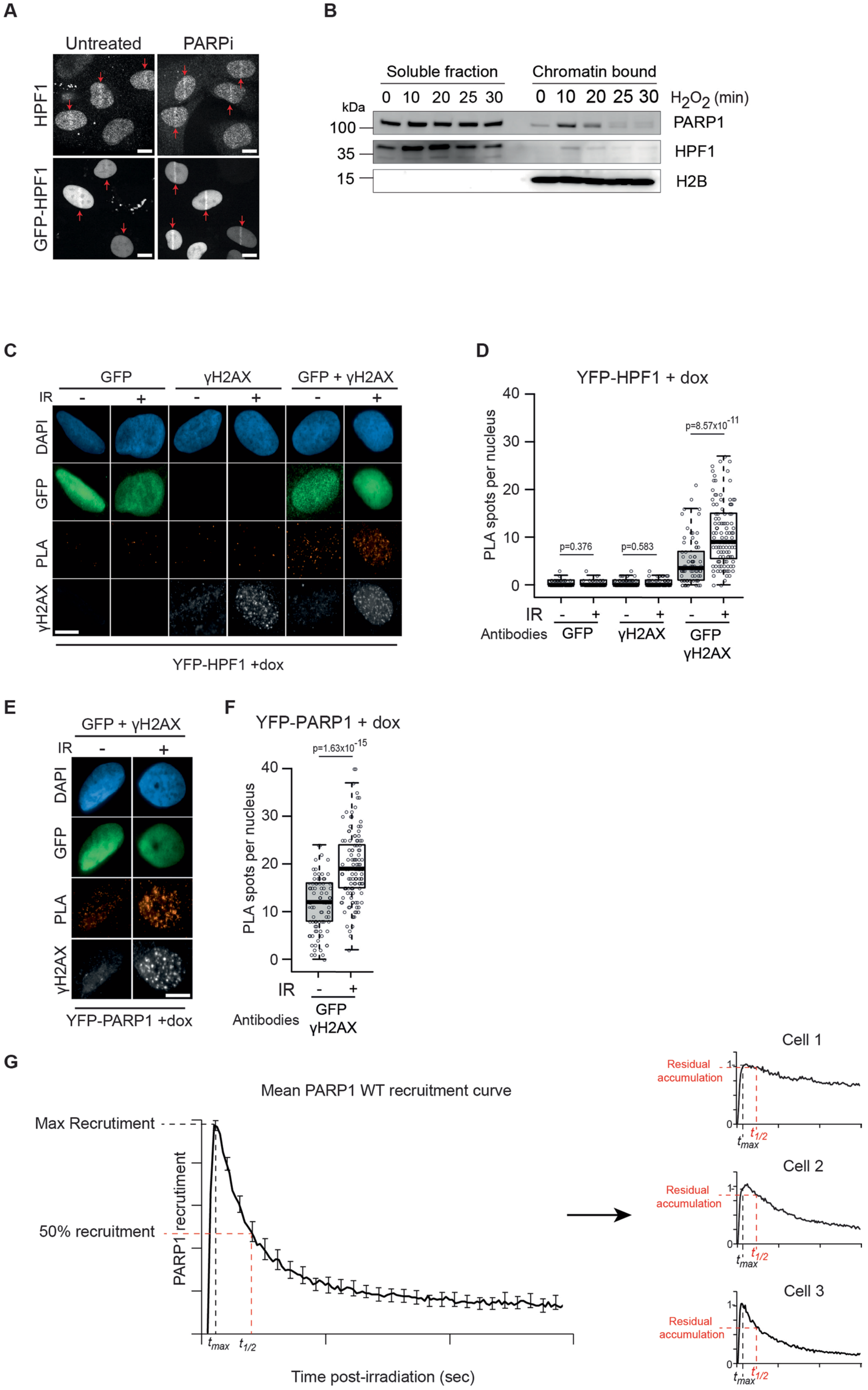

Extended Data Fig. 1 | See next page for caption.

Extended Data Fig. 1 | HPF1 recruits to sites of DNA damage. (**a**) Representative images of HPF1 recruitment to sites of DNA damage in the presence or absence of PARPi. The top panels show endogenous HPF1 recruitment while the bottom panels show GFP-HPF1 recruitment. Red arrows indicate sites of laser microirradiation with 405 nm. For HPF1 immunostaining, cells were fixed immediately after irradiation. For the GFP-HPF1 expressing cells, images were taken 120 s post-irradiation. Scale bar, 5 µm. (**b**) Analysis of PARP1 and HPF1 retention on chromatin after H_2O_2 treatment by chromatin fractionation and western blotting. Soluble and chromatin fractions are shown. H2B is used as a control demonstrating effective fractionation. (**c**–**f**) Proximity Ligation Assay (PLA) of GFP and γH2AX in U2OS Flp-In/T-Rex cells expressing doxycycline-inducible YFP-HPF1 (**c,d**) or YFP-PARP1 (**e,f**) irradiated or not with 2 Gy of ionizing radiation (IR). PLA signal was quantified as the number of PLA spots per nuclei 1 h after DSB induction. As a negative control only one primary antibody (GFP-only or γH2AX-only) was used. Representative images from >50 cells of a representative experiment from 2 independent replicates are shown. Scale bar, 5 µm (**d**) Quantification of **c**. Data from **d** are a representative of 3 independent replicates where data were collected from 49–111 cells per condition. (**f**) Quantification of **e**. Data from **f** are a representative of 3 independent replicates where data were collected from 88–119 cells per condition. (**g**) Schematic illustrating calculation of residual protein accumulation. Initially, the t_{max} and $t_{1/2}$ are determined from the mean PARP1 WT recruitment curve where t_{max} is the time where PARP1 WT recruitment is maximal, and $t_{1/2}$ is the time post-irradiaion where the recruitment has fallen to 50% PARP1 WT recruitment (Left). Then for each recruitment curve of PARP1 (WT or mutant) and HPF1, maximal recruitment was normalised to t_{max} and the residual accumulation was taken at $t_{1/2}$ (Right).

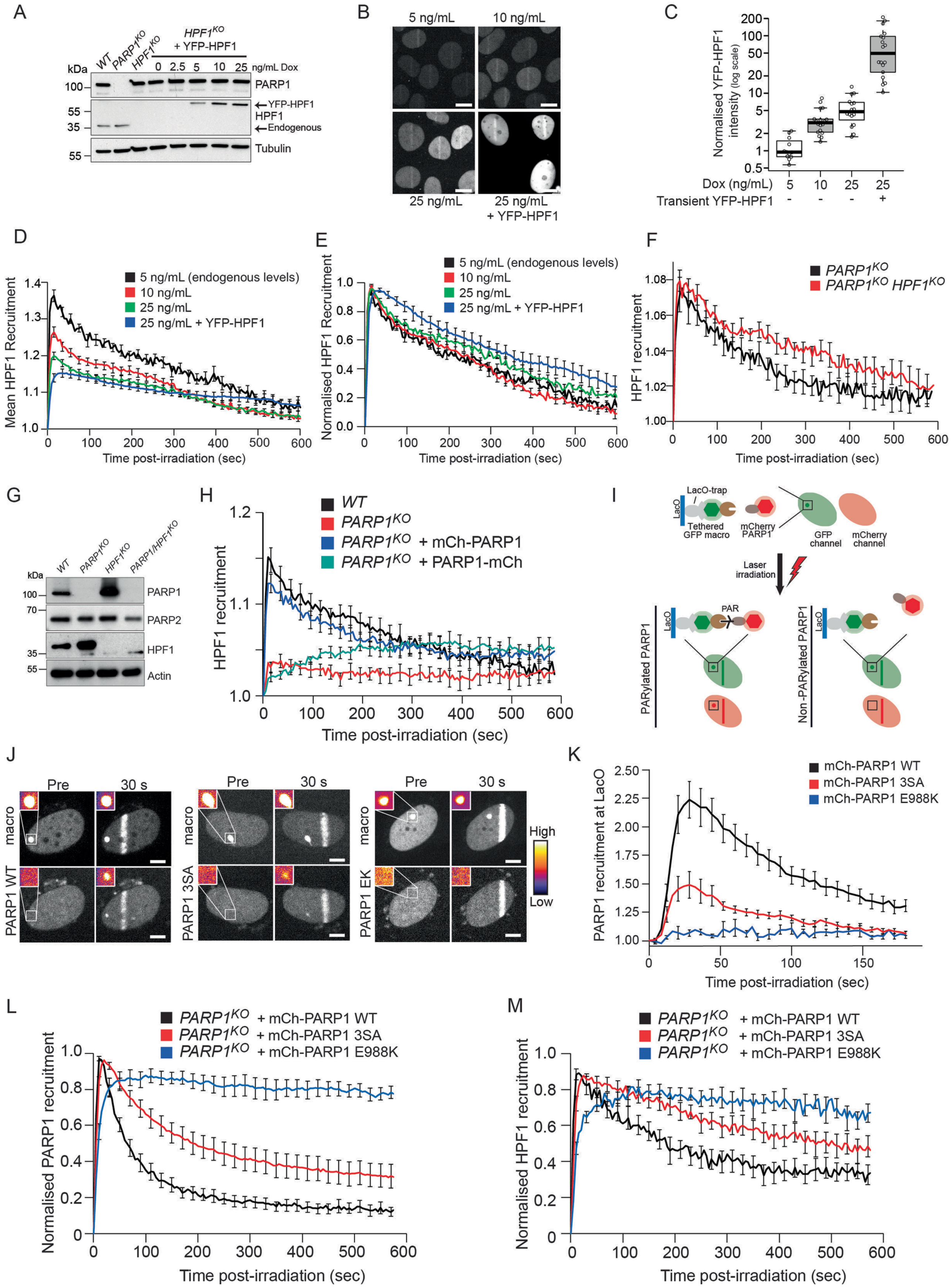

Extended Data Fig. 2 | See next page for caption.

Extended Data Fig. 2 | HPF1 recruitment to sites of damage relies on interaction with the C-terminus of PARP1. (**a**, **b**) Western blot analysis (**a**) and representative confocal images (**b**) of YFP-HPF1 expression levels in U2OS Flp-In/T-Rex *HPF1*^{KO}cells after doxycycline induced expression. Transient transfection with YFP-HPF1 was also used to further boost HPF1 expression in the presence of 25 ng/mL Doxycycline. Images were taken 30 s post 405-nm laser irradiation. Scale bar, 10 µm. (**c**) Quantification of the mean nuclear fluorescence intensity of cells from **b**. Fluorescence level is normalised to 5 ng/mL (endogenous levels of HPF1 expression according to **a**). (**d**, **e**) Mean (**d**) or normalized (**e**) recruitment kinetics of YFP-HPF1 after 405-nm laser irradiation in U2OS Flp-In/T-Rex *HPF1*^{KO}cells with different levels of doxycycline induction. Individual recruitment curves from **d** were normalised to the peak HPF1 recruitment levels. Data from **b-e** are a representative of 2 independent replicates where data were collected from 12–18 cells per condition. (**f**) Recruitment kinetics of GFP-HPF1 in *PARP1*^{KO} or *PARP1/HPF1* double knockout cells expressing mCherry-PARP1 WT. Data from **f** are a representative of 2 independent replicates where data were collected from 10–12 cells per condition. (**g**) Immunoblots of whole-cell extract from U2OS *WT*, *PARP1*^{KO}, *HPF1*^{KO} and *PARP1/HPF1* double knockout cells. (**h**) Recruitment kinetics of GFP-HPF1 to sites of DNA damage induced by 405-nm laser irradiation in *WT* or *PARP1*^{KO} cells expressing WT N-terminally (mCh-PARP1) and C-terminally tagged PARP1 (PARP1-mCh). Data from **h** are a representative of 3 independent replicates where data were collected from 12–16 cells per condition. (**i**) Schematic representation of PAR-3H assay. (**j**, **k**) Representative confocal images (**j**) or quantification (**k**) of mCherry tagged PARP1 WT, PARP1 3SA or PARP1 E988K recruitment to YFP tagged macrodomain of mH2A1.1 tethered to LacO, Pre or 30 s post-irradiation. Inset, pseudocolored according to the look-up table displayed, shows the magnified LacO array. Scale bar, 5 µm. Data from **k** are a representative of 3 independent replicates where data were collected from 13–15 cells per condition. (**l**, **m**) Normalised recruitment kinetics of mCherry tagged PARP1 (WT, 3SA or E988K) (**l**) and GFP-HPF1 (**m**) expressed in *PARP1*^{KO} cells from Fig. 1f–h. Data from **l-m** are a representative of 3 independent replicates where data were collected from 13–18 cells per condition.

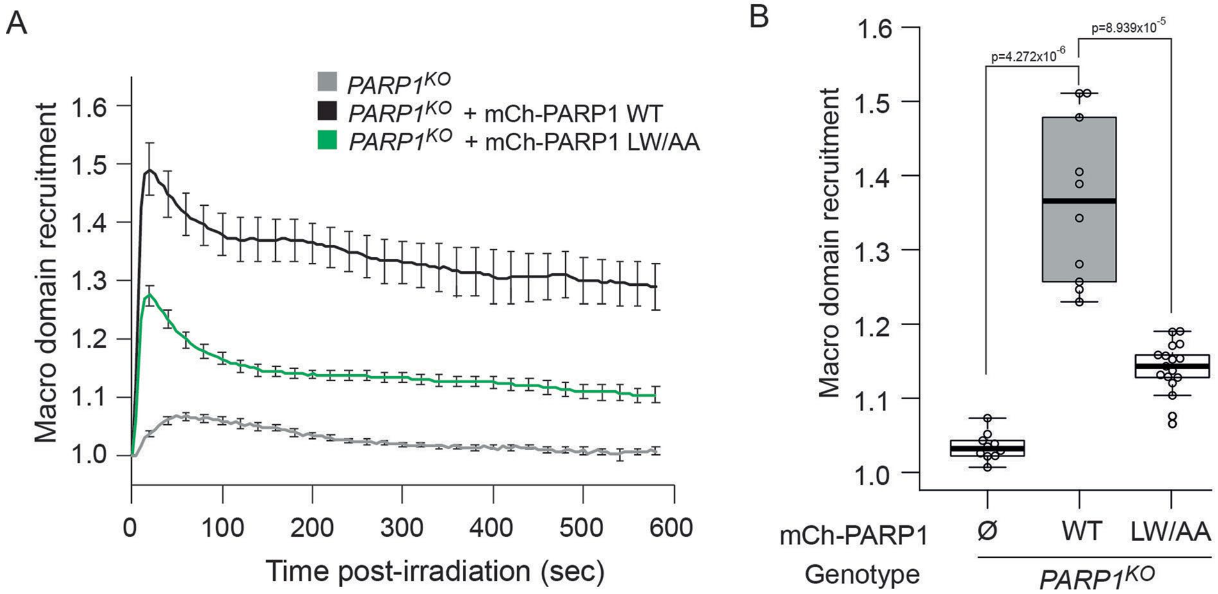

Extended Data Fig. 3 | HPF1 regulates ADP-ribosylation signaling at sites of DNA damage. (**a**) Recruitment kinetics of GFP-macrodomain of mH2A1.1 at sites of DNA damage induced by 405 nm laser irradiation, in U2OS *PARP1^{KO}* cells complemented or not with mCherry-PARP1 WT, PARP1 3SA or PARP1 LW/AA. (**b**) Quantification of mean recruitment intensity of GFP-macrodomain of mH2A1.1 at sites of DNA damage 200 s post-irradiation in *PARP1^{KO}* complemented or not with mCherry-PARP1 WT or PARP1 LW/AA mutants. Ø denotes no plasmid expression. Data from **a,b** are a representative of 3 independent replicates where data were collected from 10–17 cells per condition.

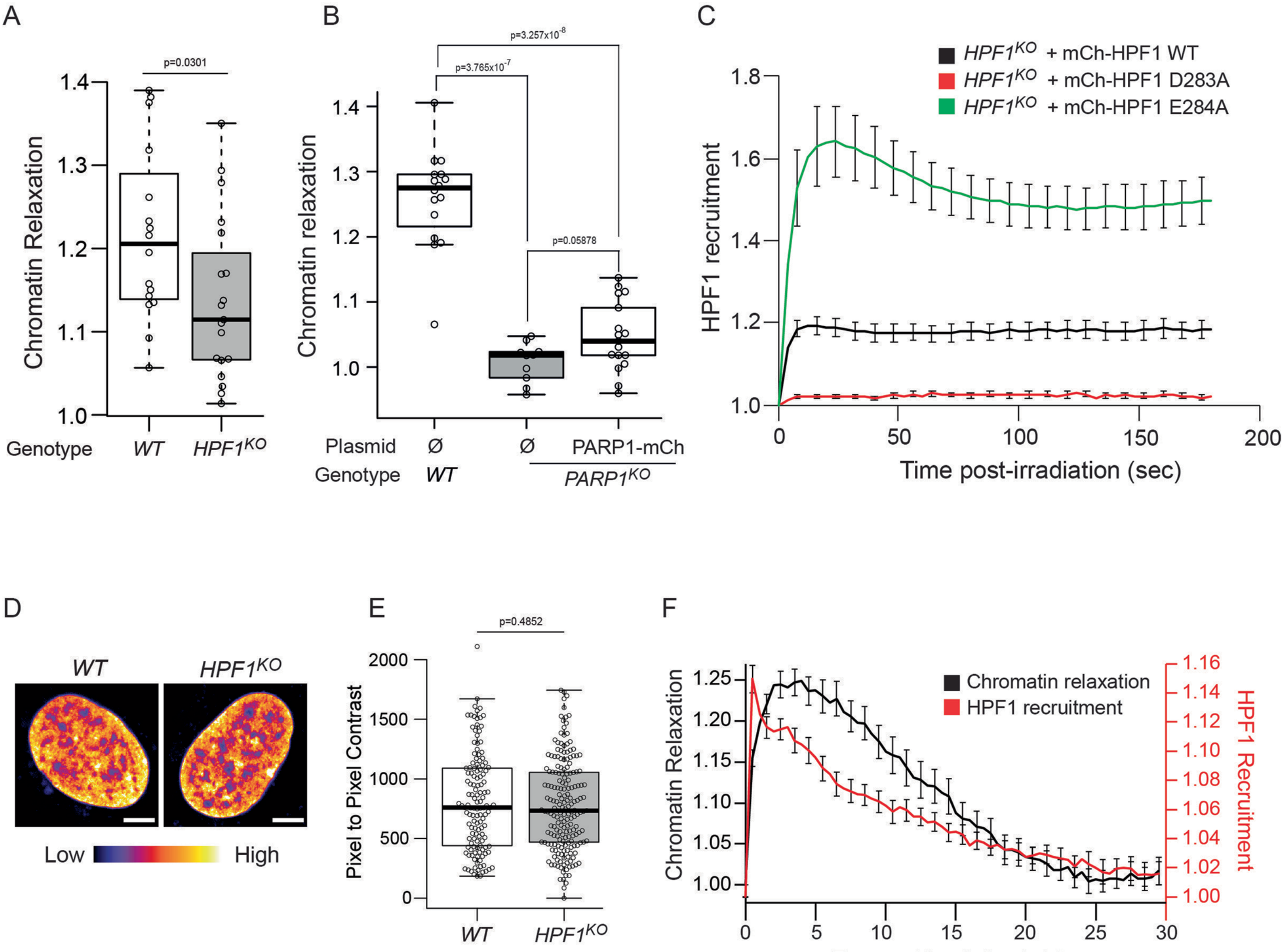

Extended Data Fig. 4 | HPF1 promotes chromatin relaxation at sites of DNA damage. (**a**) Chromatin relaxation in U2OS *WT* and *HPF1^KO* cells at 60 s post irradiation with 800 nm laser. Data from **a** are a representative of 3 independent replicates where data were collected from 16–19 cells per condition. (**b**) Chromatin relaxation in U2OS *WT* and *PARP1^KO* cells at 120 s post-irradiation at 405 nm. Cells are complemented or not with C-terminally-tagged PARP1-mCherry. Ø denotes no plasmid expression. Data from **b** are a representative of 3 independent replicates where data were collected from 10–17 cells per condition. (**c**) Recruitment kinetics of mCherry-tagged HPF1 WT and the point mutants D283A and E284A at sites of DNA damage induced by 405 nm laser irradiation in U2OS *HPF1^KO* cells. Data from **c** are a representative of 3 independent replicates where data were collected from 10–14 cells per condition. (**d**) Confocal images of U2OS *WT* and *HPF1^KO* nuclei stained with Hoechst. Scale bar, 5 µm. Images are coloured according to the lookup table below the cells. (**e**) The chromatin pattern in Hoechst-stained cells was characterised by the image contrast, calculated as the mean squared intensity difference of pixels separated by a distance of 7 pixels. Data from **e** is a representative of 2 independent replicates where data were collected from 135–190 cells per condition. (**f**) Chromatin relaxation and HPF1 recruitment kinetics at sites of DNA damage induced by 405 nm laser irradiation in WT cells overexpressing mCherry-HPF1. Data shown is mean ± SEM. Data from **f** are a representative of 3 independent replicates where data were collected from 20 cells per condition.

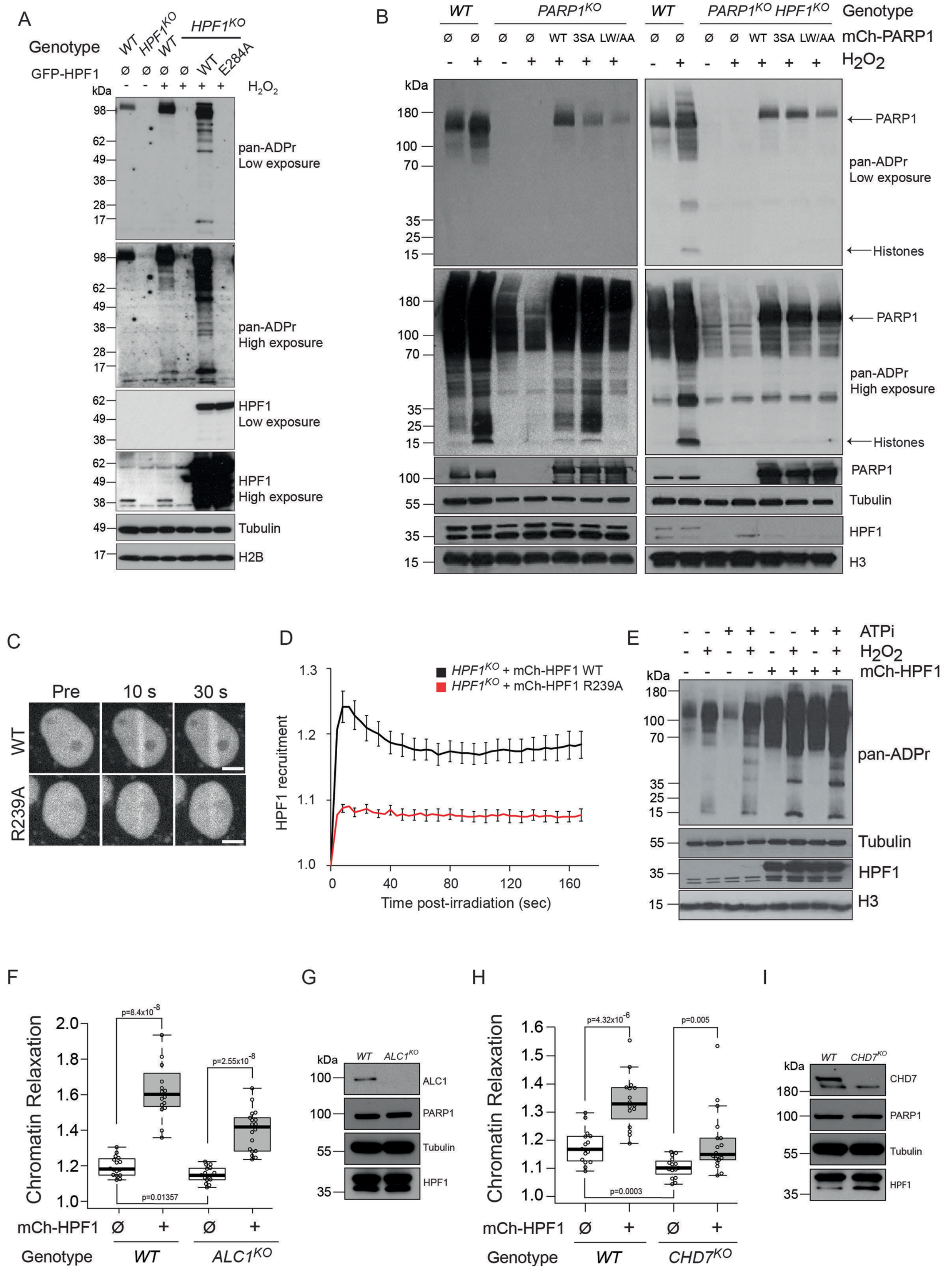

Extended Data Fig. 5 | See next page for caption.

Extended Data Fig. 5 | HPF1-dependent chromatin relaxation relies on trans ADP-ribosylation of histones rather than PARP1 auto-modification. (**a**) Western blot displaying ADPr signals, stained with a pan-ADPr antibody, in *WT* and *HPF1^{KO}* cells expressing HPF1 WT or HPF1 E284A and treated or not with H_2O_2. H2B and Tubulin were used as loading controls. (**b**) Western blot displaying ADPr signals, stained with a pan-ADPr antibody, in U2OS *WT, PARP1^{KO}* and *PARP1/HPF1* double knockout cells expressing mCherry tagged PARP1 WT, PARP1 3SA or PARP1 LW/AA and treated or not with H_2O_2. H3 and Tubulin were used as loading controls. (**c**) Representative images of the recruitment of mCherry-tagged HPF1 WT or R239A to sites DNA damage induced by 405 nm laser irradiation in U2OS *HPF1^{KO}* cells. Scale bar, 5 µm. (**d**) Recruitment kinetics of mCherry-tagged HPF1 WT or HPF1 R239A mutant at sites of DNA damage in U2OS *HPF1^{KO}* cells. Data from **d** are a representative of 3 independent replicates where data were collected from 15–16 cells per condition. (**e**) Western blot displaying ADPr signals, stained with a pan-ADPr antibody, in *WT* cells overexpressing YFP-HPF1 or not with or without ATP depletion (ATPi) after H_2O_2 damage. H3 and Tubulin were used as loading controls. (**f**) Chromatin relaxation 120 s post irradiation at 405 nm in U2OS *WT* or *ALC1^{KO}* cells overexpressing HPF1 or not. Data from **f** are a representative of 3 independent replicates where data were collected from 16–18 cells per condition. (**g**) Western blot analysis confirming knockout status of *ALC1^{KO}* cells. (**h**) Chromatin relaxation 120 s post DNA damage in U2OS *WT* or *CHD7^{KO}* cells overexpressing HPF1 or not. Data from **h** are a representative of 3 independent replicates where data were collected from 15–18 cells per condition. (**i**) Western blot analysis confirming knockout status of *CHD7^{KO}* cells.

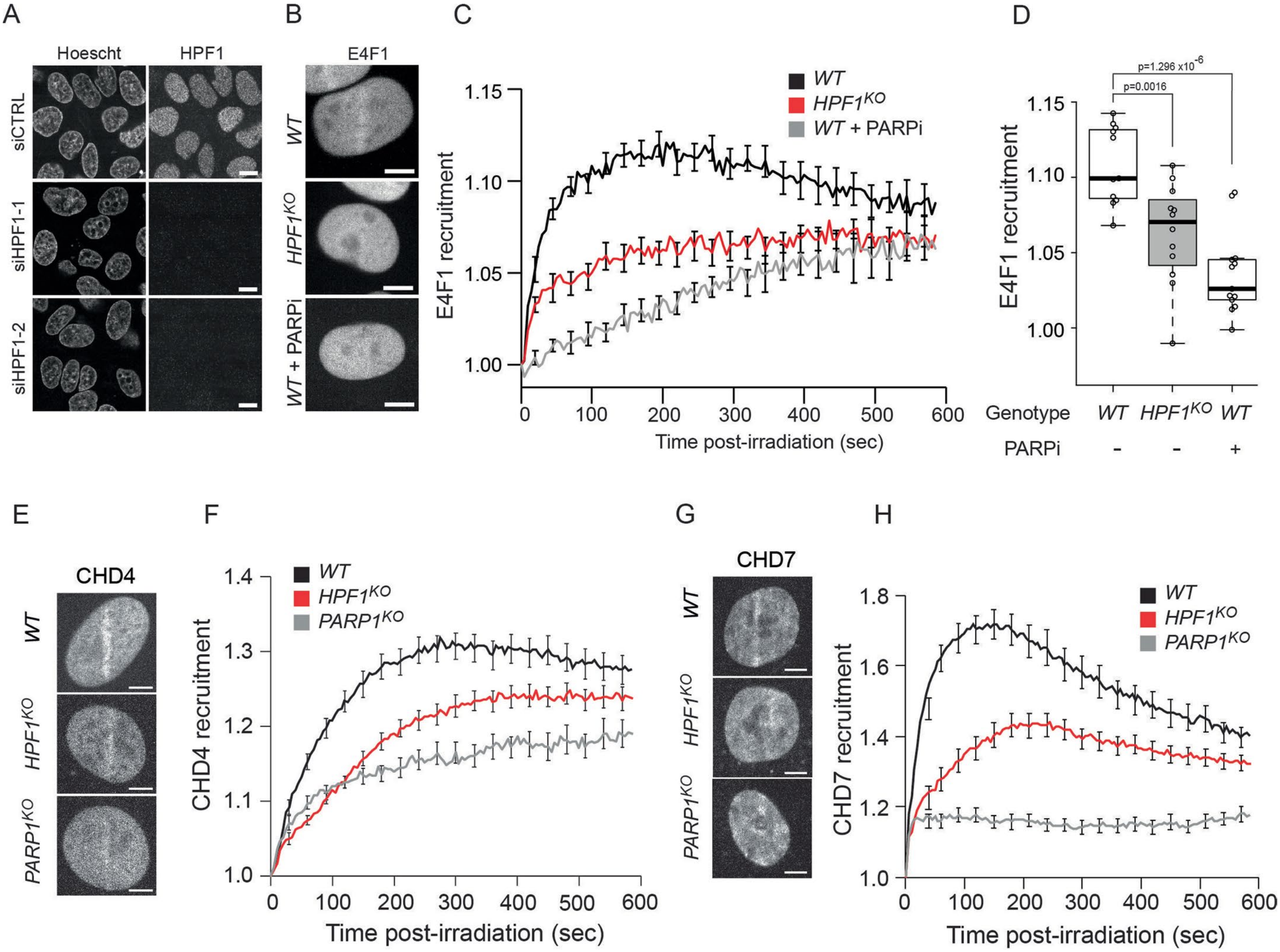

Extended Data Fig. 6 | HPF1 regulates the recruitment of DNA-binding repair factors to sites of damage. (**a**) Immunoflurosecence showing depletion of HPF1 in *ZNF384*^{KO} cells. Hoechst staining shows nuclei. Scale bar, 10 µm. (**b-d**) Representative confocal images (**b**), recruitment kinetics (**c**), and mean recruitment intensity at 200 s post-irradiation (**d**) of GFP-E4F1 at sites DNA damage induced by 405 nm irradiation in U2OS *WT* and *HPF1*^{KO} cells treated or not with PARPi. Confocal images are 200 s post-irradiation. Scale bar, 5 µm. Recruitment kinetic curves show the mean ± SEM Data from **c,d** are a representative of 3 independent replicates where data were collected from 11–13 cells per condition. (**e, f**) Representative confocal images (**e**) and recruitment kinetics (**f**) of GFP-CHD4 at sites DNA damage induced by 405 nm irradiation in U2OS *WT, PARP1*^{KO} and *HPF1*^{KO} cells. Confocal images are 200 s post-irradiation. Scale bar, 5 µm. Recruitment kinetic curves show the mean ± SEM. Data from **f** are a representative of 3 independent replicates where data were collected from 13–22 cells per condition. (**g, h**) Representative confocal images (**g**) and recruitment kinetics (**h**) of GFP-CHD7 at sites DNA damage induced by 405 nm irradiation in U2OS *WT, PARP1*^{KO} and *HPF1*^{KO} cells. Confocal images are 200 s post-irradiation. Scale bar, 5 µm. Recruitment kinetic curves show the mean ± SEM. Data from **h** are a representative of 3 independent replicates where data were collected from 13–16 cells per condition.

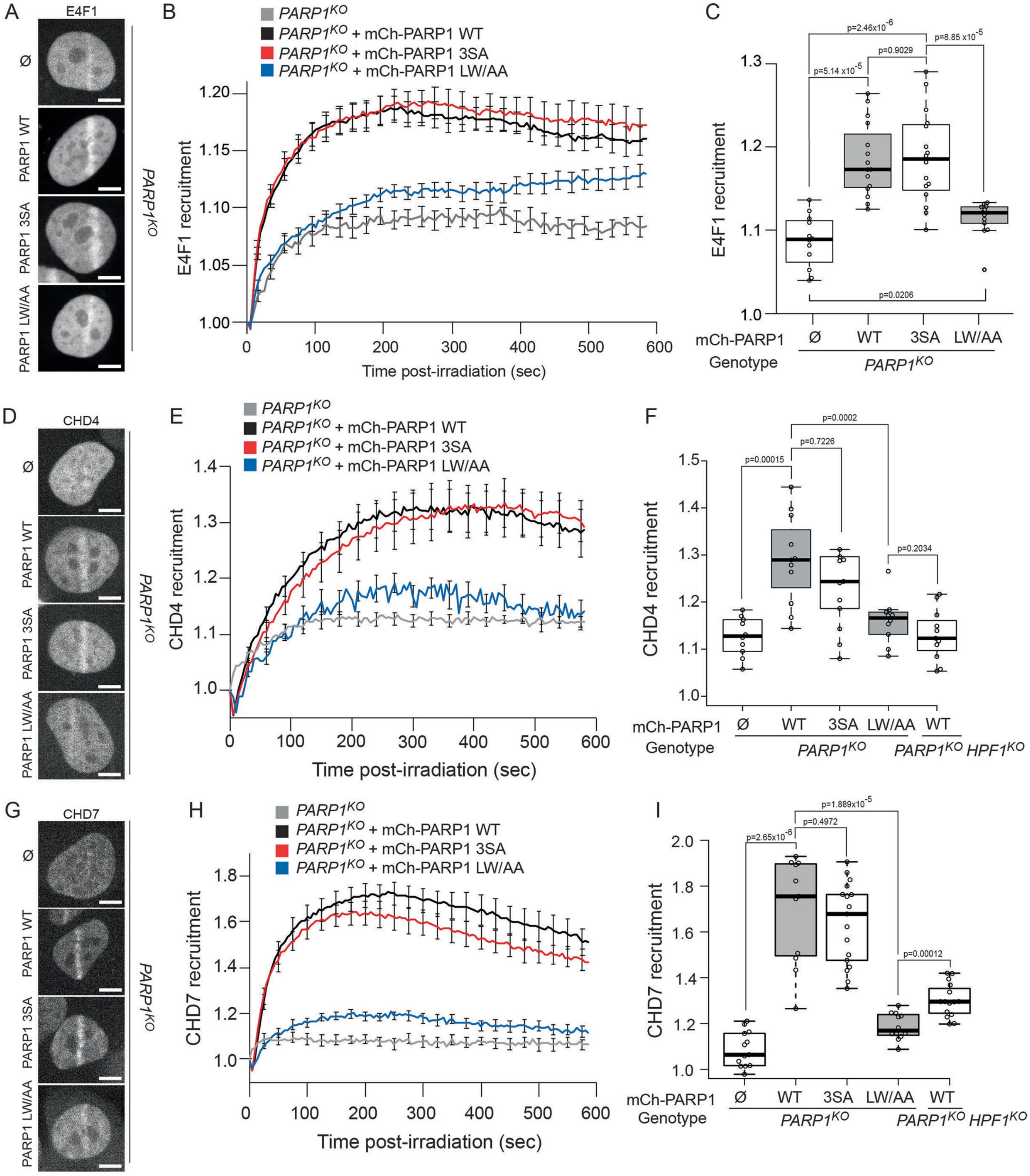

Extended Data Fig. 7 | See next page for caption.

Extended Data Fig. 7 | HPF1-dependent recruitment of DNA-binding repair factors to sites of damage is promoted by histone ADP-ribosylation. **(a–c)** Representative confocal images (**a**), recruitment kinetics (**b**), and mean recruitment intensity at 200 s post-irradiation (**c**) of GFP-E4F1 at sites DNA damage induced by 405 nm irradiation in U2OS *PARP1^{KO}* cells complemented or not with mCherry-PARP1 WT, PARP1 3SA or PARP1 LW/AA. Confocal images are 200 s post-irradiation. Scale bar, 5 µm. Recruitment kinetic curves show the mean±SEM. Data from **b,c** are a representative of 3 independent replicates where data were collected from 12–16 cells per condition. **(d-f)** Representative confocal images (**d**), recruitment kinetics (**e**), and mean recruitment intensity at 200 s post-irradiation (**f**) of GFP-CHD4 at sites DNA damage induced by 405 nm irradiation in U2OS *PARP1^{KO}* or *PARP1/HPF1* double knockout cells complemented or not with mCherry-PARP1 WT, PARP1 3SA or PARP1 LW/AA mutants. ∅ denotes no plasmid expression. Confocal images are 200 s post-irradiation. Scale bar, 5 µm. Recruitment kinetic curves show the mean ± SEM. Data from **e,f** are a representative of 3 independent replicates where data were collected from 10–13 cells per condition. **(g-i)** Representative confocal images (**g**), recruitment kinetics (**h**), and mean recruitment intensity at 200 s post-irradiation (**i**) of GFP-CHD7 at sites DNA damage induced by 405 nm irradiation in U2OS *PARP1^{KO}* or *PARP1/HPF1* double knockout cells complemented or not with mCherry-PARP1 WT, PARP1 3SA or PARP1 LW/AA mutants. ∅ denotes no plasmid expression. Confocal images are 200 s post-irradiation. Scale bar, 5 µm. Recruitment kinetic curves show the mean ± SEM. Data from **h,i** are a representative of 3 independent replicates where data were collected from 10–12 cells per condition.

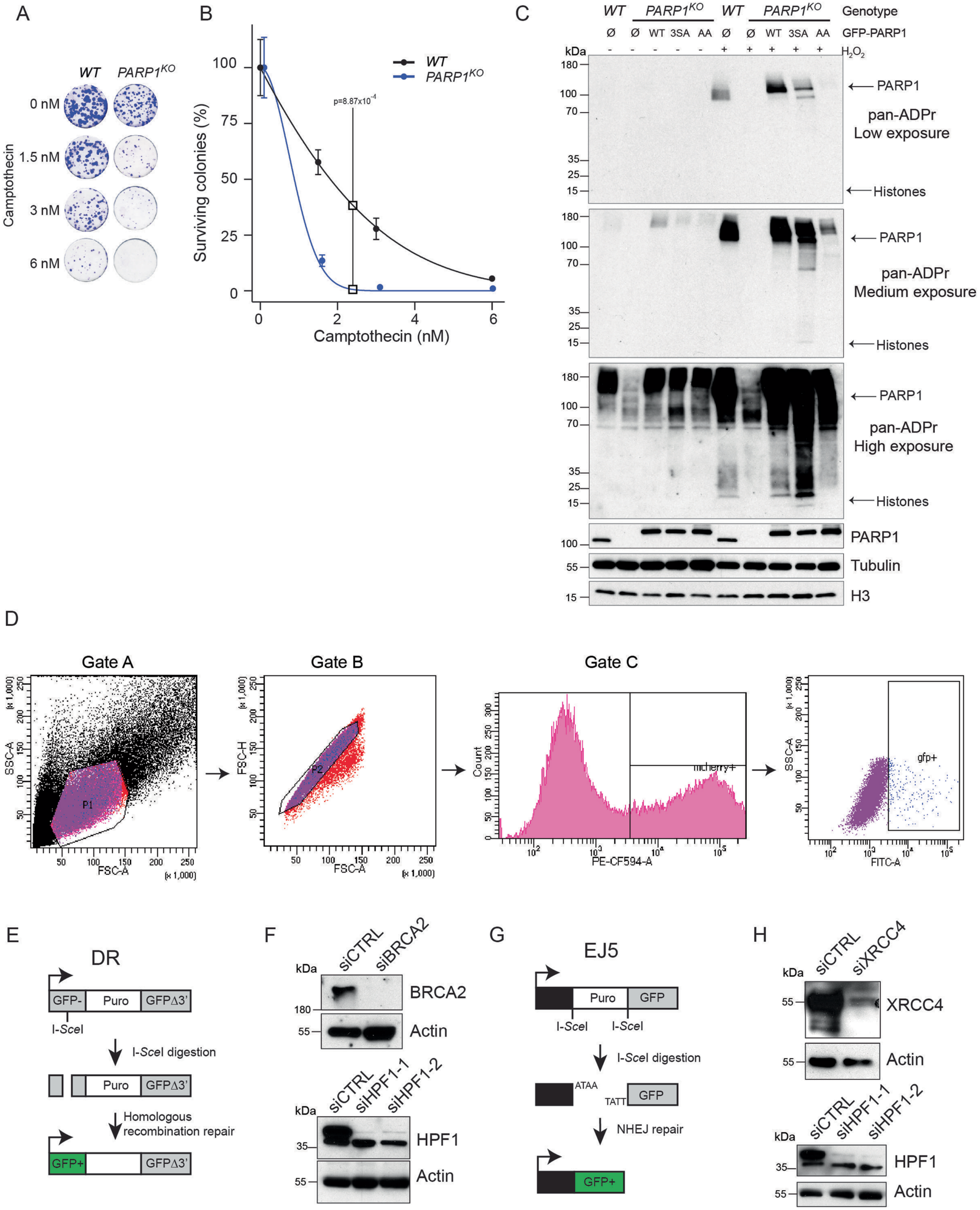

Extended Data Fig. 8 | See next page for caption.

Extended Data Fig. 8 | HPF1 promotes efficient DNA repair. (**a**, **b**) Representative images of clonogenic assay (**a**) and cell survival curves (**b**) for *WT* and *PARP1^{KO}* cells upon continuous camptothecin treatment. Data are a representative of 3 independent replicates. (**c**) Western blot displaying ADPr signals, stained with a pan-ADPr antibody, in U2OS *WT, PARP1^{KO}* and *PARP1^{KO}* cells stably expressing GFP tagged PARP1 WT, PARP1 3SA or PARP1 LW/AA and treated or not with H_2O_2. H3 and Tubulin were used as loading controls. (**d**) Gating strategy used to analyze DNA repair efficiency. Gate A was used to select living cells: SSC-A scatter against FSC-A. Gate B was used to remove of doublets: FSC-H scatter against FSC-A. The mCherry positive population was selected in Gate C where mCherry positive cells had above background PE-CF594-A signal. The GFP-positive population (FITC-A) was selected and counted from mCherry positive cells in Gate C (final panel). (**e**) Schematic representation of the HR reporter assay (DR). After cleavage with I-SceI, the double-strand-breaks repaired by HR results in GFP expression. (**f**) Representative immunoblots showing the knockdown efficiency of BRCA2 and HPF1 in DR cells. Actin is used as a loading control. (**g**) Schematic representation of the NHEJ reporter assay (EJ5). Double cleavage by I-SceI removes the Puro cassette and the repair of the double-strand-break by NHEJ allows GFP expression. (**h**) Representative immunoblots showing the knockdown efficiency of XRCC4 and HPF1 in EJ5 cells. Actin is used as a loading control.